Summer 8-1-2023

High-power laser cooling and temperature-dependent fluorescence studies of ytterbium doped silica

Brian Topper

Follow this and additional works at: https://digitalrepository.unm.edu/ose_etds

 Part of the Atomic, Molecular and Optical Physics Commons, Optics Commons, and the Other Engineering Commons

Recommended Citation

Brian Topper

Candidate

Optical Science and Engineering

Department

This dissertation is approved, and it is acceptable in quality
and form for publication:

Approved by the Dissertation Committee:

Dr. Arash Mafi

Dr. Ganesh Balakrishnan

Dr. Doris Möncke

Dr. James Thomas

High-power laser cooling and temperature-dependent fluorescence studies of ytterbium doped silica

BY

Brian Topper

B.S., Physics, University of Richmond, 2015
M.S., Materials Science and Engineering, Alfred University, 2020

DISSERTATION

Submitted in Partial Fulfillment
of the Requirements for the Degree of
Doctor of Philosophy

Optical Science and Engineering
The University of New Mexico
Albuquerque, New Mexico

August, 2023

DEDICATION

In memory of
Mansoor Sheik-Bahae
(1956-2023)

The work of this dissertation stands on the shoulders of this great researcher and exceptional man. Mansoor's guidance and vast experience in solid-state laser cooling made the rapid progress in silica cooling described in this dissertation possible.

ACKNOWLEDGMENTS

Gratitude is due in abundance to the many mentors, instructors, colleagues, and classmates that have surrounded me on this journey of scientific research. Explicit thanks is owed to my doctoral supervisor, Arash Mafi for providing the space, support, and encouragement to first crawl and eventually maneuver with confidence in an optics laboratory.

At the University of New Mexico, Dr. Alexander Neumann's shared experience, conversation, and camaraderie requires explicit acknowledgement. Thanks are also due to Drs. Mansoor Sheik-Bahae, Alexander Albrecht, Mostafa Peysokhan, and Cody Bassett. Special thanks also goes out to Drs. Angel Flores and Thomas Schreiber for helpful discussions on fiber amplifier construction. And of course, the subject of this work is ytterbium doped silica glasses, to which Drs. Stefan Kuhn and Thomas Schreiber as well as their team in Jena, Germany were kind enough to provide.

During the work carried out towards this dissertation, a parallel research life was lived in the realm of glass science. This was made possible by the engaging collaborations with Dr. Doris Möncke, the crew at Alfred University, and colleagues in Greece, Germany, New York, and Illinois.

Enduring the trials and tribulations of graduate school would not have been possible without the continuous support and encouragement of my family - thank you.

High-power laser cooling and temperature-dependent fluorescence studies of ytterbium doped silica

by

Brian Topper

B.S., Physics, University of Richmond, 2015
M.S., Materials Science and Engineering, Alfred University, 2020
Ph. D., Optical Science and Engineering, The University of New Mexico, 2023

ABSTRACT

Experimental observation of optical refrigeration using ytterbium doped silica glass in recent years has created a new solution for heat mitiga-tion in high-power laser systems, nonlinear fiber experiments, integrated photonics, and precision metrology. Current efforts of different groups focus on compositional optimization, fiber fabrication, and investigating how much silica can be cooled with a laser. At the start of this work, the best effort in laser cooling ytterbium doped silica saw cooling by 6 K from room temperature. This dissertation follows the experimental ef-forts that culminated in the increase of this initial record by one order of magnitude. Comprehensive spectroscopic studies were carried out to fully understand the potential of the available samples. The external quantum efficiency was measured to be 99% for two Yb-doped silica rods containing at least 6 times more Al than Yb. Current laser cooling results employing a homemade 100 W fiber amplifier operating at 1032 nm have resulted in laser cooling a 1 mm diameter Yb, Al co-doped silica glass rod in vac-uum by 67 K from room temperature. These results indicate that with some additional optimization, silica will soon surpass Yb:ZBLAN as the coolest glass. Detailed temperature-dependent and site-selective fluores-cence studies carried out in this work show that obtaining relevant laser cooling parameters for $Yb:SiO_2$ is not straightforward. For example, mean fluorescence wavelength measurements at room temperature vary between 1008 and 1012 nm, depending on the excitation wavelength. Regarding the Yb^{3+} site environment, the zero-phonon line transition is well-described by two band components spaced approximately 40 cm^{-1} apart, suggesting the possibility of two main local site environments of the Yb^{3+} ions.

Contents

LIST OF FIGURES

LIST OF TABLES

1 Introduction

1.1 History and fundamentals

C.V. Raman is given credit for first detailing that when a material is exposed to light, its molecules scatter a small fraction of the incident photons inelastically. This inelastic scattering results in lower energy (Stokes) and higher energy (anti-Stokes) photons [1]. Shortly after, Peter Pringsheim postulated that the anti-Stokes fluorescence may be used to decrease the temperature of a material [2]. In 1968, Kushida and Geusic carried out solid-state anti-Stokes fluorescence (ASF) pumping experiments using an undoped and a Nd^{3+} doped yttrium aluminum garnet (YAG) crystal [3]. A Nd:YAG crystal was used as the pump laser operating at 1064 nm providing up to 200 W of power. Experiments were done at ambient pressure conditions and the crystals subject to the pump light were supported by thin needles to decrease the conductive heat load. Relative to the undoped crystal, the Nd-doped crystal heated *less*. The temperature change versus pump data from Reference [3] is reproduced in Figure 1. ASF of the Nd^{3+} was ascribed as the reason for the lower temperature in the Nd:YAG sample at a given incident pump power and the authors claimed the first observation of optical refrigeration. However, no net cooling was observed.

Slightly prior to these Nd:YAG experiments, Weinstein described a "technical efficiency", η, of a lamp converting heat into light as *the ratio of the power leaving the lamp in the form of luminescence radiation to the power supplied to the lamp in the form of work* [4]. In the experimental configuration for solid-state optical refrigeration used by Kushida and Geusic, this could be defined as a cooling efficiency, η_c,

$$\eta_c = \frac{P_{out}}{P_{in}}, \tag{1}$$

where P_{out} is the fluorescence (luminescence radiation) leaving the crystal (lamp) and P_{in} is the laser light pumping the crystal (power supplied). Kushida and Geusic elab-
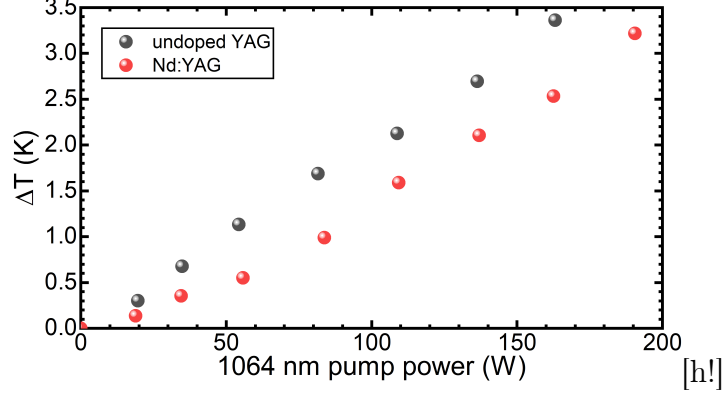
Figure 1: Observation of decreased heating in Nd:YAG crystal attributed to the heating from impurties, as in the undoped YAG case, coupled with anti-Stokes fluorescence cooling by the Nd^{3+} ions. Adapted from Kushida and Geusic, Reference 3.

orate on the actual realization such a solid-state "lamp", *"In order to observe net cooling, the possible heating mechanisms of Stokes fluorescence, nonradiative transitions, and the absorption of laser radiation by impurity ions in the refrigerator crystal are required to be weak compared with the cooling by anti-Stokes fluorescence"*. The first element of this statement alluding to *"the possible heating mechanisms of Stokes fluorescence"* is addressed by choosing λ_p, the wavelength of the pump source providing P_{in}, to be longer than the mean wavelength of the fluorescence emission lineshape, λ_f, so that $\lambda_p > \lambda_f$. λ_f is the mean value of the ensemble of radiative decays as an excited ion returns to the ground state and can be obtained by calculating the first moment of the experimentally measured emission lineshape, $S(\lambda)$,

$$\lambda_f = \frac{\int \lambda\, S(\lambda)\, d\lambda}{\int S(\lambda)\, d\lambda}. \tag{2}$$

Ignoring, for now, the nonradiative transitions and purity issues raised by Kushida and Geusic, an ideal form of the cooling efficiency can be written in more accessible terms as

$$\eta_c(\lambda_p) = \frac{\lambda_p}{\lambda_f} - 1. \tag{3}$$

Equation 3 simply states that as λ_p is increasingly detuned further away from λ_f in the red-tail of the absorption spectrum, $\alpha_r(\lambda)$, the cooling efficiency will increase. Since optical absorption of radiation by an ion is often described as a Lorentzian oscillator, in the purely mathematical sense, this implies a finite, albeit small, absorption of impinging radiation even far away from resonance. One may then be led to think that a very high value of η_c can be obtained by simply taking $\lambda_p >>>> \lambda_f$. However, as alluded to by Kushida and Geusic, in physically realizable materials there will always be (at least for the foreseeable future) some amount of impurities giving rise to some degree of a background absorption, α_b. It is most desirable to have as much P_{in} as possible resonantly absorbed by the ions that have the potential to radiate ASF. Absorption by impurities not only decreases the available energy for the ASF process, but can serve as a source of internal heat generation. The relative magnitudes of the useful absorption to the background absorption can be introduced as the absorption efficiency, $\eta_{abs}(\lambda)$,

$$\eta_{abs}(\lambda) = \frac{\alpha_r(\lambda)}{\alpha_r(\lambda) + \alpha_b}, \tag{4}$$

necessitating the modification of Equation 3,

$$\eta_c(\lambda_p) = \frac{\lambda_p}{\lambda_f}\eta_{abs}(\lambda_p) - 1. \tag{5}$$

This tells us that we actually want to make λ_p not too far from λ_f, so as to keep

$\eta_{abs}(\lambda)$ near 1. The caveat comes in addressing the last facet of the conditions for net cooling as given by Kushida and Geusic, that the nonradiative transitions ought to be weak. An ion in its excited state can take two possible avenues to return to the ground state - a radiative decay or a nonradiative decay. Only radiative decays, i.e. emitted photons, that *escape* the bulk solid have any hope at contributing to net optical refrigeration. Nonradiative decays arising from multi-phonon relaxation, clustering, and quenching of the excited state by impurities (hydroxyl species, rare-earth ions, transition metal ions) will all hinder the ASF cooling process. The term encompassing these processes is dubbed the external quantum efficiency, η_{ext},

$$\eta_{ext} = \frac{\eta_e W_r}{\eta_e W_r + W_{nr}},\tag{6}$$

where W_r and W_{nr} represent the radiative and nonradiative decay rates, respectively, and η_e is the escape efficiency. The escape efficiency is dependent on the reabsorption coefficient and the sample geometry. The reabsorption coefficient is calculated from the overlap between the normalized emission lineshape and the resonant absorption coefficient spectrum. Since the former is intrinsic and the latter scales directly with the total ion dopant density, N_T, a more highly doped sample will result in a higher reabsorption coefficient, as might be expected. Sample geometry will determine the ability of radiated photons to exit the sample-environment interface and not be internally reflected. In this work, the quantity η_{ext} will be measured directly in Chapter 3, but the interested reader is directed to the works by Heeg *et al.* [5] as well as Ruan and Kaviany [6] for further discussion on η_e. Alas, η_{ext} is appended directly to the main product in Equation 5,

$$\eta_c(\lambda_p) = \frac{\lambda_p}{\lambda_f}\eta_{abs}(\lambda_p)\eta_{ext} - 1.\tag{7}$$

Assuming a high purity material so that α_b is extremely small compared to $\alpha_r(\lambda)$

yielding a near unity η_{abs} in the vicinity of λ_f, the wavelength invariant η_{ext} sets a lower limit on the choice of λ_p to induce net cooling, dubbed the cross-over wavelength by Bowman *et al.* [7]. Together, η_{ext} and $\eta_{abs}(\lambda)$ set the short wavelength and long wavelength bounds, respectively, for net cooling.

The quantities appearing in Equation 7 will be called upon throughout this work. For a more mathematical and less hand-waving derivation of Equation 7, see References [8, 9]. The construction of the cooling efficiency term in this manner is judged to be more accessible and prepares us well for later where, in Chapter 5, we will ultimately learn that the application of this Equation 7 in a predictive manner to ytterbium doped silica glass (the main character of the story here) needs to be considered carefully.

1.2 Net cooling

The accidental discovery of stable, multi-component fluoride glasses by Poulain *et al.* led to a boom in the study of halide glass [10]. Research in the 1980s was driven by the theoretical low loss and good infrared transmission of halide glasses [11]. Subsequently, in the 1990s, the research focused heavily on the use of halide glasses for optically active gain media following the discovery of their high rare-earth solubility [11]. With the know-how to produce ultra-pure rare-earth doped materials, solid-state laser cooling was reported for the first time in Yb:ZBLANP by Epstein and co-workers at Los Alamos National Lab [12]. These first experiments observed cooling by $0.3\,\mathrm{K}$ from room temperature at a pump wavelength of $1015\,\mathrm{nm}$ and $\eta_c(\lambda = 1015\,\mathrm{nm})$ was estimated to be about 2%. The temperature change as measured with a calibrated thermal camera, normalized to the input pump power, versus the pump wavelength as reported by Epstein *et al.* is reproduced in Figure 2. Foreseen applications of this new era of 'net cooling' included mainly the cryogenic cooling of infrared detectors and other devices. The potential for an all solid-state, vibration-free, liquid-free cool-
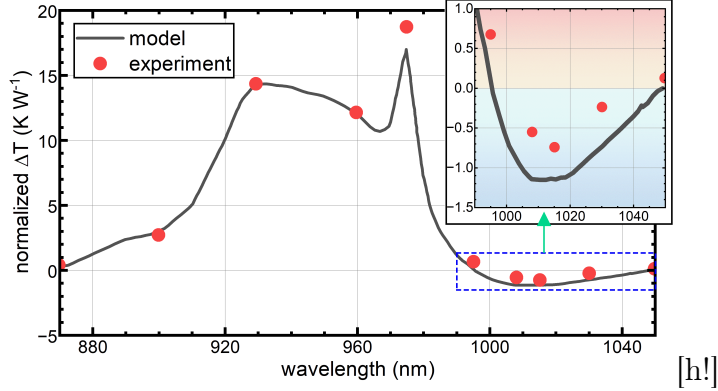
Figure 2: Normalized temperature change versus wavelength displaying the first observation of net cooling in Yb:ZBLANP glass. Adapted from Epstein *et al.*, Reference 12.

ing device led to the suggestion that the technology would be useful for space-based applications, which is indeed still a focus of research efforts and advancing closer to implementation [13, 14].

In the following years, ytterbium doped fluoride glasses were cooled by 16 K (1997), then by 21 K (1998) and then by an impressive 65 K (1999) [15, 16, 17]. The 65 K cooling result by Gosnell [17] was achieved with a 1 wt% Yb^{3+} doped multimode fiber with 170/250 micron core/clad diameters. The cooling sample was placed in vacuum to remove the convective heat load and supported by 125 μm diameter silica fibers to minimize the conductive heat load. This left only the radiative heat load of the surrounding environment. The sample was pumped with 2.2 W at λ_p=1015 nm from a Ti:Sapphire laser that had been mode scrambled by propagation through 4 m of graded index fiber so as to reduce the intensity profile within the cooling medium. A double-pass geometry reflected the unabsorbed pump back into the sample to increase the overall available pump. The temperature was measured by a least-squares comparison of the fluorescence lineshape after the sample reached a steady-state with known temperature dependent emission spectra obtained using a closed-cycle cryostat. This experimental approach is very similar to what will be used in the chapters ahead.

A few more years would pass before optical cooling of Yb:ZBLAN down to 208 K was reported in 2005 [18]. For this demonstration, a high vacuum environment and fiber support system were used, as in Gosnell's work [17]. The Yb^{3+} concentration was increased by a factor of 2 relative to the 65 K cooling Yb:ZBLAN sample. Pump power was also increased to 10 W and best results were obtained at λ_p=1026 nm. A fiber preform was employed (as opposed to a fiber) with an 8 mm diameter doped core and an 11 mm diameter undoped cladding. A self-contained multi-pass scheme was implemented by depositing dichroic mirrors on the end faces of the preform with a clean pinhole opening through which the pump light could be launched into the sample. The radiative load of the chamber onto the sample was reduced by lining the chamber with a foil with high absorption at the fluorescing wavelengths and low emissivity at long thermal wavelengths. To date, this remains the best result in optical cooling of a vitreous material.

Thereafter, researchers vying for a cryogenic all solid-state cooler redirected their attention to crystalline materials [19, 20, 21] which has yielded immense success [22, 23, 24]. The lack of inhomogeneous broadening in crystalline materials permits more resonant absorption at a given pump power and wavelength. Additionally, fluoride crystals containing an optically inactive lanthanide, such as yttrium in $YLiF_4$ for example, allow direct substitution of the active refrigerator ion. This allows high dopant densities before the onset of clustering which in turn allow a larger degree of cooling. To date, the coldest temperature achieved by solid state optical refrigeration is in crystalline Yb:$YLiF_4$ down to 91 K [20]. Infrared detectors have been cooled down to cryogenic temperatures [22]. Payloads have, as of this writing, been cooled down to 124.7 K [24] and researchers are closing in on their goal of optically refrigerating a payload to 123 K which will be applied to vibration-free cooling of silicon reference cavities at NIST [25].

Recent years have also seen concentrated efforts to use laser cooling for radiation
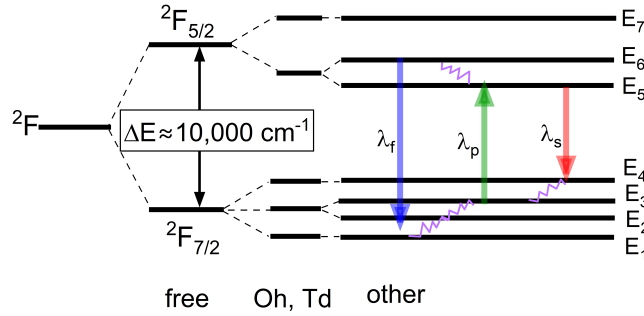
Figure 3: Stark levels of Yb^{3+} with site symmetry decreasing from left to right. All degeneracy is lifted in the glassy state, making "other" the schematic of interest here. Superimposed over the Stark sublevels are the straight arrows corresponding to key radiative events in the laser cooling and radiation balanced processes. Jagged lines represent nonradiative events.

balanced lasers (RBL) and radiation balanced amplifiers (RBA) [23, 26, 27]. Bowman first proposed the idea of an RBL in 1999, where the anti-Stokes fluorescence (ASF) offsets the heat generated during lasing operation due to the quantum defect and parasitic absorption [28]. Heat mitigation by ASF was then observed in Yb:YAG rod lasers in 2010 [7] and used to make an RBL in a Yb:YAG disk laser in 2019 [23]. Bowman's concept is illustrated in Figure 3 in the context of an Yb^{3+} system. The system is pumped at λ_p from a thermally populated sublevel of the lower manifold to the lowest level of the upper manifold. The upper manifold thermalizes rapidly. The radiative relaxation down to the lower manifold is represented by the mean fluorescence wavelength previously discussed, λ_f. The lower level then thermalizes, repopulating the sublevels depleted by previous absorption events at λ_p. This is the basic laser cooling cycle. If feedback is introduced into the system so that laser oscillation is created at a longer wavelength, λ_s, then this process will result in some amount of heating. When the net heat caused by lasing at λ_s is offset by the fluorescence characterized by λ_f, then the situation is termed "radiation balanced".

Employing heat mitigation by ASF has been of particular interest in the context of fiber lasers. While fiber lasers routinely output kW level single mode beams [29,

30, 31], highly stable multi-kW class fiber lasers with narrow linewidths suitable for beam combination are currently challenged by temperature rise in the core resulting in the deleterious phenomenon of transverse mode instability (TMI) [32] or catastrophic material damage due to thermal lensing.

As discussed above, fluoride glasses of the ZBLAN family have been laser cooled repeatedly with great success [33] and were an early candidate for fiber RBLs [34]. On the other hand, the high degree of polymerization and strong Si−O bonds make vitreous silica superior to fluoride systems, such as the ZLBAN family, with respect to mechanical and chemical durability. On a practical note, the prospect of easily splicing into existing silica fiber components is also highly desirable for the construction of compact, real world devices using the RBL/RBA idea.

1.3   Optical refrigeration of silica

Despite its ubiquity in optics, laser cooling of silica evaded early attempts [35]. Exploiting ASF in a silica host was not an obvious solution at first, due to the high phonon energy of the fully polymerized SiO_4 tetrahedral unit, the antisymmetric stretch of which peaks at $\nu_{as} = 1100\,\mathrm{cm}^{-1}$ [36] (see Figure 4). Note that this is about twice that of the more highly coordinated Zr polyhedra in ZBLAN glasses ($\nu_{as} = 500\,\mathrm{cm}^{-1}$) [37]. In Figure 4, the emission spectra of Yb^{3+} (red lines) and the infrared absorption spectra (black lines) for SiO_2 and ZBLAN are shown [34, 38, 37]. The separation between the ground and excited state of Yb^{3+} is mostly insensitive to the host, as is typical of rare-earth ion f−f transitions in general due to the lack of participation of the f shell electrons in local bonding. This separation for ytterbium is typically around $10{,}200\,\mathrm{cm}^{-1}$. As a result, it would appear that since the silica host environment only requires half the phonons to bridge the Yb^{3+} excited state relative to ZBLAN, an η_{ext} approaching unity would be much harder to achieve.

A reevaluation of ytterbium doped silica by Mobini et al. in 2018 argued that
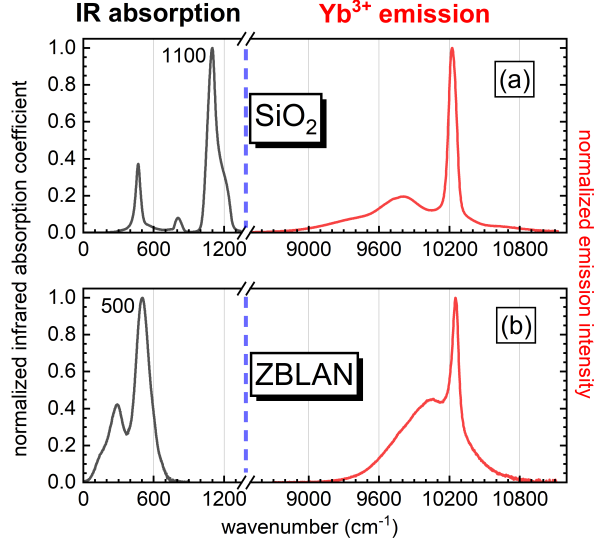
Figure 4: (a) Normalized infrared absorption coefficient spectrum of SiO_2 (black) and normalized spontaneous emission spectrum of Yb:SiO_2 (red). (b) Normalized infrared absorption coefficient spectrum of ZBLAN (black) and normalized spontaneous emission spectrum of Yb:ZBLAN (red). All measurements were made at room temperature. Infrared spectra are from Ref. 38 (SiO_2) and Ref. 37 (ZBLAN).

in fact, there is no fundamental mechanism prohibiting the optical refrigeration of Yb:silica [39]. This was swiftly followed with experimental observations of laser cooling silica by tens to hundreds of mK from room temperature, by independent groups, using fiber preforms [40] and drawn fibers [41]. A later experiment [42] on a preform from Ref. [9] reported cooling in-vacuum by $6\,K$ after machining away roughly 95% of the passive cladding to decrease the associated thermal load, optimizing the wavelength of the pump light, and doubling the power from the experiments in Ref. [9]. Around the same time, an investigation into the influence of glass composition by the authors of Ref. [41] led to better performing fibers [43] which were then utilized to construct the first silica RBL [27] and RBA [26].

Analysis does not suggest silica will necessarily outperform materials like ytterbium doped yttrium lithium fluoride (YLF) for optical refrigeration [44, 39]; however, silica offers unique solutions with its optical isotropy, ruggedness, and formability (i.e. fibers, substrates, microspheres) and the resulting interest is abundant [45]. De-

vices have been fabricated exploiting anti-Stokes fluorescence cooling of ytterbium doped silica [46, 26, 27]. Other efforts have explored various composition ranges and co-doping schemes [47, 48, 49], including introduction of the ytterbium via fluoride nanoparticles [50]. Design and modeling of novel fiber architectures have also been investigated [51, 52, 53, 54]

This dissertation describes the most aggressive experimental endeavor to date in terms of power cooling Yb^{3+} doped silica. First, the record at the start of this work is tripled, with cooling by $18\,K$ from room temperature presented in Chapter 2. A two-fold improvement is described in Chapter 4, where cooling by $41\,K$ is recorded. Finally, the current record of laser cooling silica by $67\,K$ starting from room temperature is demonstrated in Chapter 6, which represents one complete order of magnitude increase since the start of this project. The in-between Chapters 3 and 5 relate to the characterization of the samples used in Chapter 2, 4 and 6. Chapter 3 describes measurements of the external quantum efficiency using the Laser Induced Thermal Modulation Spectroscopy (LITMoS) test. Chapter 5 reports an in-depth site-selective excitation study of Yb^{3+} doped silica and discusses the implications for the future characterization of ytterbium doped silica for laser cooling applications. Concluding remarks will be given in Chapter 7 with a condensed summary of experimental results of this work as well as recommendations for future work.

2 Era of double digit silica cooling

2.1 Samples

Our journey begins with the arrival of two sets of samples courtesy of the Fraunhofer Institute for Applied Optics and Precision Engineering, Jena, Germany. The samples were silica glass rods 1 mm in diameter drawn from preforms fabricated by the modified chemical vapor deposition method. The preforms consisted of a >3 mm diameter doped core and >14 mm undoped cladding. To increase the cooling effect in the samples, the undoped cladding was mostly removed from the preform and only a thin layer of passive cladding was left surrounding the active core material. Afterward, the preforms were drawn to rods with an outer diameter of 1000 μm and a doped core diameter of 900 μm. Aluminum (as $AlCl_3$), ytterbium (as $Yb(thd)_3$) and fluorine were added simultaneously to the core by the gas-phase doping technique [55]. The aluminum was employed to increase the critical quenching concentration of the ytterbium [56, 57]. Fluorine was added to the core of the preform for precise refractive index control. The core region, where the dopants are present, is 900 micron in diameter and is surrounded by a passive undoped layer. The refractive index step between the core and the cladding is precisely controlled to give a low numerical aperture. Glasses of this type in standard 20/400 fiber dimensions have been used in high-power fiber lasers [31]. Although the numerical aperture is crucial for single-mode operation of 20/400 fiber, it is of minor relevance for the 900 micron core rod-type geometry. Relevant properties are listed in Table 1.

2.2 Experimental

In these early studies with the new rod samples, in-vacuum power cooling experiments were carried out using the setup that was employed by Peysokhan *et al.* in the experiments that saw cooling of a cylinder by 6 K from room temperature [42]. See

Table 1: Material properties of Yb doped fibers

Fiber	A	B
Codopants	Al, F	Al, F
Yb_2O_3 (mol%)	0.15	0.12
Yb^{3+} density (10^{25} atoms/m^3)	6.56	5.26
Al:Yb ratio	6:1	8.3:1
NA_{core}	0.06	0.05
$D_{core}/D_{cladding}$ (μm/μm)	900/1000	900/1000

Figure 5 for a visualization. Approximately 45 mW of 1035 nm light from a continuous wave (CW) Ti:Sapphire (Ti:S) laser is coupled through free space to a single mode fiber with an objective lens. A custom-built fiber amplifier increases the signal power, providing an output up to 20 W. The amplifier consisted of a single stage architecture. An inline fiber isolator protects the Ti:S from back reflection. A 99:1 tap coupler placed after the isolator monitors forward and backward propagation. The forward seed, originally in single-mode (SM) HI1060 fiber (6 micron core, 125 micron cladding - "6/125"), is expanded with a mode field adapter to then utilize a large mode area (LMA) 25/250 fiber architecture. A pump and signal combiner couples 978 nm multimode (MM) pump light into the cladding in a forward-pumping configuration. A forward-pumping fiber amplifier configuration is one in which the pump and signal light propagate in the same direction, as opposed to a counter-pumping configuration that will be used in Chapter 6. The 25/250 fiber, now with signal in the core and pump in the cladding, is spliced to a Yb-doped 25/250 fiber. As the MM pump is absorbed in the doped core of the gain fiber, the signal is amplified. A cladding mode stripper (CMS) removes residual pump in the cladding following the end of the gain fiber. An acid-etched CMS is employed. A passive (undoped) 25/250 fiber serves as the delivery conduit.

The amplified signal serves as the input power to the Yb-doped silica rod subject for cooling. The output is collimated and passed through 1000 nm long pass filters (LPF). The LPFs are important for two aspects. First, some low NA pump light
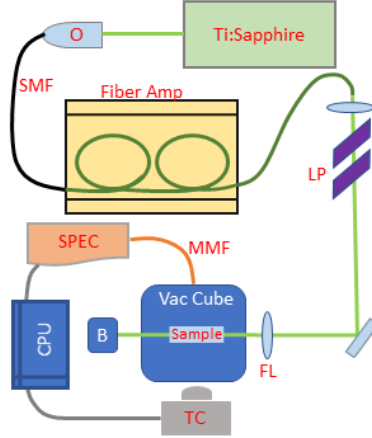
Figure 5: Schematic of experimental set up with 1035 nm source (Ti:Sapphire), 20x objective lens (O), single mode fiber (SMF), custom-built fiber amplifier (Fiber Amp), two long pass filters (LP), focusing lens (FL), vacuum chamber (Vac Cube) containing the sample and thermally transparent windows for observation, thermal imaging camera (TIC), multimode fiber (MMF) connected to a spectrometer (SPEC), beam block (B), and computer for data collection (CPU).

is constrained to the core of the fiber and so is not removed by the CMS. Second, spontaneous emission is generated in the gain medium, and all light at wavelengths within the Yb absorption cross-section that are shorter than the cross-over wavelength will heat the sample.

The doped fiber (Fiber A - Table 1) is supported by undoped thin fused silica fibers to minimize conductive heating. To minimize convective heating, the doped fiber and sample holder are placed in an evacuated chamber where, for these experiments, a pressure of about 5×10^{-5} torr was achieved. The input is coupled to the enclosed fiber by a 10 cm focal length lens. Perpendicular to the axis of the fiber are two windows for real-time observation. One window is thermally transparent KCl for recording the temporal behavior of the fiber with a thermal imaging camera (TIC). The other window is fused silica through which discrete measurements of the fluorescence are taken by collecting the emitted light with a multimode fiber connected to a silicon CCD line spectrometer (Ocean Optics).

The temperature difference is defined as $\Delta T = T - T_0$ where T_0 is taken to be the
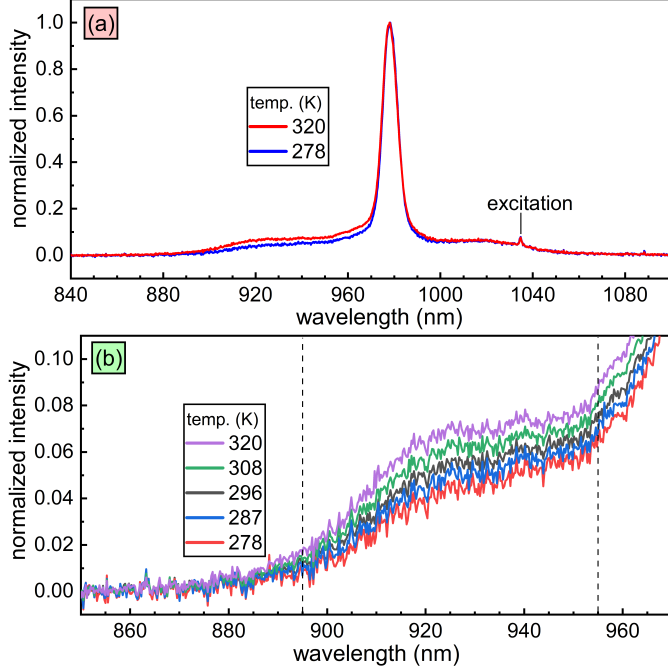
Figure 6: (a) Fluorescence spectra recorded above and below room temperature with CCD spectrometer. (b) Short wavelength region used for thermometry shown for selected wavelengths.

ambient temperature of $296\,\text{K}$. TIC was used to track the evolution of the temperature, or at least the initial change in temperature due to the limited dynamic range of the camera. The TIC available saturates at roughly $6\,\text{K}$ below ambient temperature, and is therefore inadequate for recording greater cooling than has been reported up until now. To record cooling beyond $\Delta T = 10\,\text{K}$, differential luminescence thermometry (DLT) was employed [58, 42]. DLT exploits the temperature-dependence of the luminescence spectral form. A calibration is performed, and the experimental results are then quantified through this. Aspects of this calibration process are shown in Figure 6.

The sample was placed on a temperature controlled plate and excited at $\lambda_{exc} = 1035\,\text{nm}$, the same wavelength used for cooling experiments. The emitted fluorescence was focused with a pair of lenses into a multimode fiber and sent to the OceanOptics CCD Spectrometer. The temperature of the plate was varied between 278 K and 320
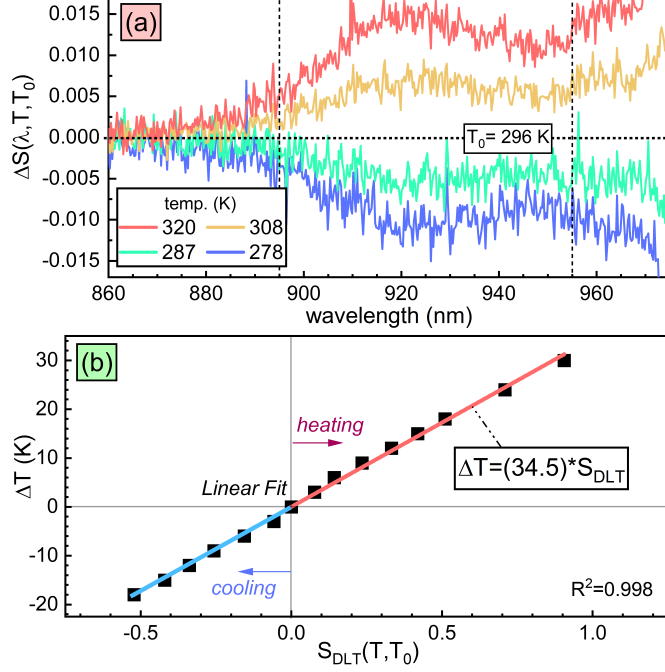
Figure 7: (a) Difference spectra relative to room temperature for selected temperature measurements (b) Relation between temperature change and integrated difference spectrum shown with linear fit.

K. After equilibrium was established, the average of 1000 scans of 100 millisecond integration times were taken with an approximate 0.5 nm resolution. To correct for changes in the background, the mean over the interval [200,800] nm was calculated and this value was subtracted from the entire spectrum. The baseline corrected spectrum was then normalized to the maximum intensity value.

Figure 6a shows normalized measurements approximately $20\,\mathrm{K}$ above (red) room temperature (RT) and below RT (blue). The main change is observed in the short wavelength range ($\lambda < 960\,\mathrm{nm}$). This region is highlighted in Figure 6b for several temperatures. The two vertical dashed lines highlighted at $895\,\mathrm{nm}$ and $955\,\mathrm{nm}$ indicate the region used for thermometry.

The normalized difference spectra (Figure 6a) is defined as

$$\Delta S(\lambda, T, T_0) = \frac{S(\lambda, T)}{S_{max}(T)} - \frac{S(\lambda, T_0)}{S_{max}(T_0)} \tag{8}$$

16
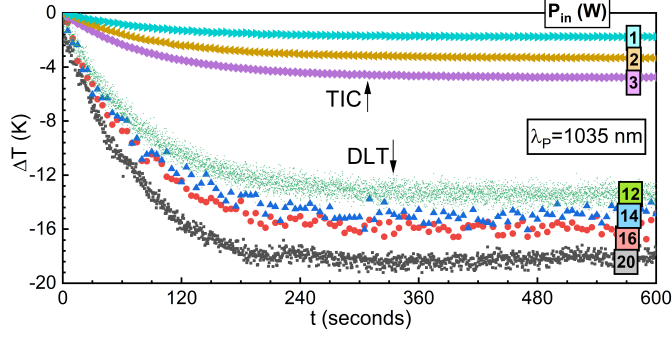
Figure 8: Experimentally measured cooling curves for Sample A from in-vacuum experiments using $\lambda_p = 1035$ nm.

The change in temperature is found to be linearly proportional to the integrated difference in spectral density given by

$$S_{DLT}(T, T_0) = \int_{\lambda_1}^{\lambda_2} |\Delta S(\lambda, T, T_0)| d\lambda \tag{9}$$

such that $\Delta T = \alpha\, S_{DLT}$ with $\alpha = 34.5 \pm 0.4$ K for fiber A ((Figure 6b).

2.3 Results and discussion

Figure 8 displays experimentally measured temporal cooling behavior for Sample A cooling trials performed in-vacuum with different input pump powers. Trials with ≤ 3 W were measured with the TIC and trials using ≥ 12 W were measured with DLT. For trials measured with thermal camera and low pump powers, ΔT_{max} is taken as the average ΔT over the interval of 10 to 25 minutes. For trials measured with DLT and higher pump powers, ΔT_{max} is taken as the average over the interval of 5 to 7 minutes as sometimes an upward drift in the temperature was observed to take place beyond 7 minutes. ΔT_{max} for all experimental trials is plotted in Figure 9

Focusing on the best results, the temperature difference measured by the TIC is compared to the temperature difference by DLT in Fig. 10 for a 20 W pump power incident on the sample held under vacuum. In Fig. 10, it can be seen that, in the absence of convective heating contributions, both DLT (black line) and TIC (blue

17
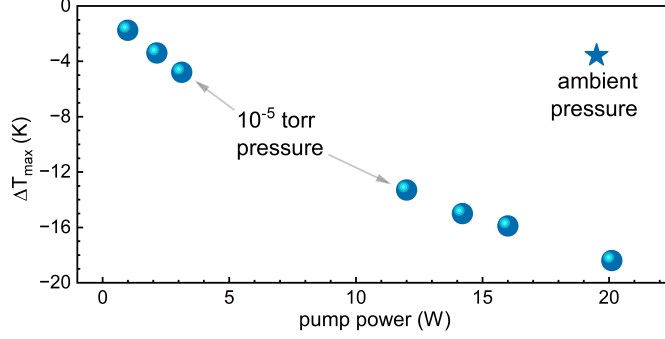
Figure 9: ΔT_{max} of sample A for different pump powers using $\lambda_p = 1035\,\text{nm}$. Spheres represent high vacuum measurements and the star represents a measurement made at ambient pressure.

circles) measurements record nearly the same rate of cooling up to about 25 seconds of lapsed time. At this point, the thermal imaging camera becomes saturated. When the experiment was performed in-air (red line), the maximum temperature difference achieved was less than $4\,\text{K}$ and so the TIC was able to reliably track the cooling of the fiber with $20\,\text{W}$ of input power under atmospheric pressure. Despite the maximum ΔT being reduced by about a factor of 5 for the in-air measurement, the onset of cooling for in-air and in-vacuum trials coincides for the initial $\sim 5\,\text{seconds}$, $\Delta T \approx 1.3\,\text{K}$, before the air measurement deviates. The dashed green line in Fig. 10 represents the application of the following exponential form to the data,

$$\Delta T(t) = \Delta T_{max}(e^{-t/\tau_c} - 1). \tag{10}$$

The time constant in the exponential of Eq. (10) may be defined by

$$\tau_c = \frac{\rho V c_v}{4\epsilon\sigma T_0^3 A}, \tag{11}$$

where the values are listed in Table 2. For sample A, evaluation of Eq. (11) gives $\tau_c = 81\,\text{s}$. This agrees well with the average experimental value $\tau_c = 84\pm3\,\text{s}$. Taking $\tau_c = 84\pm3\,\text{s}$ and determining the ΔT_{max} from the TIC or DLT data, Eq. (10) was

18
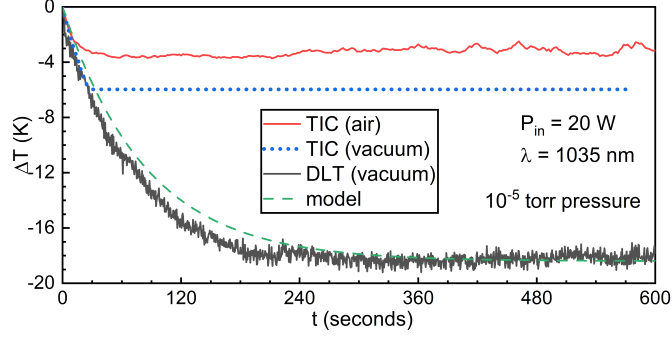
Figure 10: Comparison of temperature measurements of sample A pumped with 20 W of 1035 nm light in both vacuum (TIC-blue and DLT-black) and atmospheric (TIC-red) pressure conditions. The green line corresponds to the application of Equation 10 to the DLT in vacuum data.

Table 2: Sample parameters

parameter	sample A
A	$1.6 \times 10^{-4}\,\mathrm{m^2}$
V	$3.9 \times 10^{-8}\,\mathrm{m^3}$
c_v	$741\,\mathrm{J \cdot kg^{-1} \cdot K^{-1}}$
ϵ	0.85
ρ	$2.2 \times 10^3\,\mathrm{kg \cdot m^{-3}}$
σ	$5.67 \times 10^{-8}\,\mathrm{W \cdot m^{-2} \cdot K^{-4}}$
T_0	$296\ \mathrm{K}$

found to model the experimental data quite well.

Next the absorbed power, P_{abs}, is determined with the Beer-Lambert law

$$P_{abs} = P_{in}\mathsf{T}_{tot}(1 - e^{-\alpha_r z}). \tag{12}$$

P_{in} is the pump power measured before the focusing lens, T_{tot} is the total transmission coefficient of the experimental arrangement, z is the length of the sample (5 cm), and α_r is the resonant absorption coefficient. T_{tot} is the product of the transmission of the focusing lens ($\mathsf{T}_l = 0.998$), the transmission of the chamber window ($\mathsf{T}_{cw}=0.92$), and the transmission into the glass sample after accounting for Fresnel losses at the surface ($\mathsf{T}_g = 0.96$) so that $\mathsf{T}_{tot} = \mathsf{T}_l\mathsf{T}_{cw}\mathsf{T}_g$.

The resonant absorption coefficient at the wavelength of interest was found by
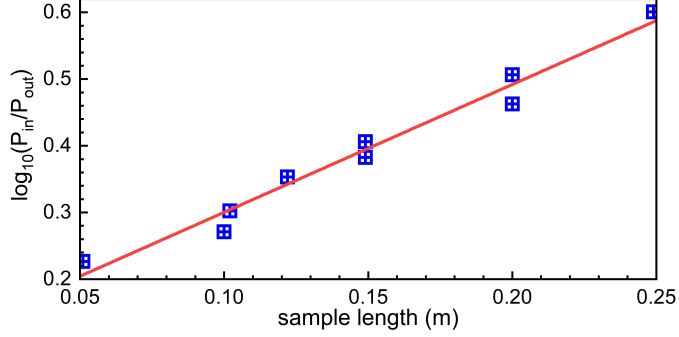
Figure 11: Experimentally measured relationship between input power and output power at $\lambda = 1035\,\text{nm}$ for different sample lengths (blue squares) with linear fit (red line). Each square represents the average of 6 individual measurements. Error bars are smaller than the size of the symbol.

measuring samples of the same composition having lengths between $0.05\,\text{m}$ and $0.25\,\text{m}$. A fiber pigtailed butterfly laser diode was used as the light source. The collimated beam was coupled into the sample core using a $20\times$ objective lens. The power was measured after the objective lens without the sample, and then again at the output end of the sample. Power was adjusted via varying the current of the laser diode, with the thermoelectric cooler settings adjusted to maintain a near constant wavelength. From all measurements, $\lambda_{\text{input}}=1035.3\pm0.3\,\text{nm}$, which is assumed to give a very accurate approximation for quantities at $\lambda=1035\,\text{nm}$, where cooling experiments were performed using the Ti:S laser source. Employing the Beer-Lambert law once more, the logarithm of the ratio between the input power, P_{in}, and the output power, P_{out}, is related to the various sample lengths, z, (Figure 11). A linear fit of the form $\epsilon + \alpha_r \cdot z$ indirectly gives the coupling efficiency, ζ, for the measurements, $\zeta = (1 - \epsilon) * 100 = 89.1\%$, and the absorption coefficient, $\alpha_r = 1.92 \pm 0.04\,\text{m}^{-1}$.

As seen clearly in Figure 9, the magnitude of the cooling of sample A in-vacuum was found to increase with increasing absorbed power. With the absorbed power now known for each trial, the slope of the $\Delta T(t)$ curves at $t = 0$ is inspected (Figure 12) to find the cooling efficiency, η_c, of sample A at $\lambda_p = 1035\,\text{nm}$ wavelength via

$$\eta_c(\lambda_p = 1035\,\text{nm}) = \frac{-\rho\text{Vc}_\text{v}}{\text{P}_\text{abs}}\partial_\text{t}\Delta\text{T}|_\text{t=0}. \tag{13}$$

$\eta_c(\lambda_p = 1035\,\text{nm}) = 1.2 \pm 0.1\%$ for sample A at $\lambda_p = 1035\,\text{nm}$ (Figure 13).
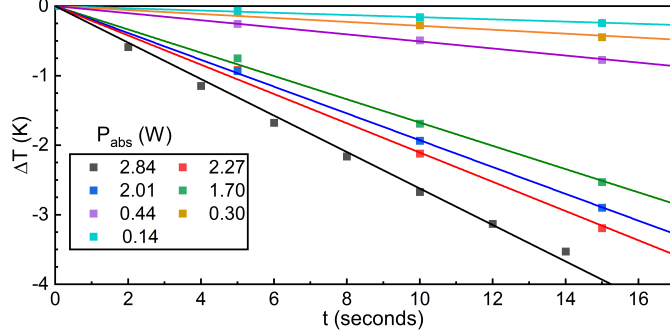
Figure 12: Experimentally measured onset of cooling (symbols) with linear fits over of the plotted range (lines).
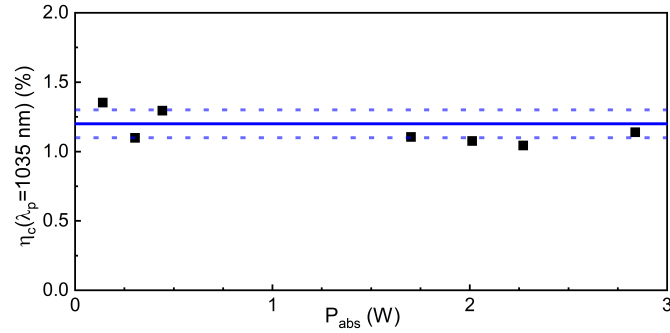
Figure 13: Calculated cooling efficiency (symbols) for sample A with respect to absorbed power shown with the mean (solid blue line) and the standard deviation (blue dotted line).

For sample B, experiments were conducted under ambient pressure conditions by colleagues at Fraunhofer Institute for Applied Optics and Precision Engineering. Data acquisition was carried out with a FLIR T540 thermal camera. The notable result of these experiments was the observation of cooling by $6.3\,\text{K}$ from room temperature using $185\,\text{W}$ of a $1033\,\text{nm}$ pump (Fig. 14). Figure 15, plots the maximum cooling as a function of pump power from all experiments on sample B at Fraunhofer IOF.

21
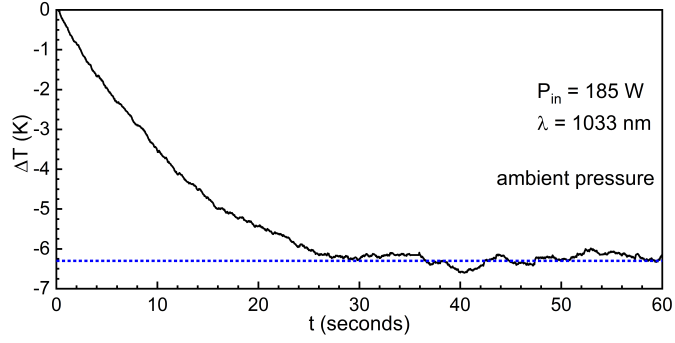
Figure 14: Temporal cooling behavior of sample B pumped with $185\,\mathrm{W}$ of $1033\,\mathrm{nm}$ light under ambient pressure conditions. The dotted horizontal line is positioned at $-6.3\,\mathrm{K}$ to aid the eye.
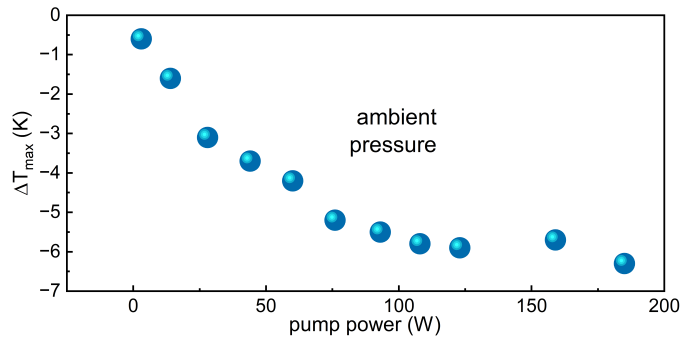
Figure 15: ΔT_{max} of sample B for different pump powers at ambient pressure using $\lambda_p = 1033\,\mathrm{nm}$.

2.4 Conclusions

In summary, optically cooling silica to more than 18 K below room temperature has been achieved. This was achieved for sample A by placing the doped glass rod in-vacuum and pumping with 20 W of 1035 nm light. Compared to the previous work by Peysokhan *et al.*[42], increasing the Yb^{3+} concentration from 0.12 mol% to 0.15 mol%, significantly reducing the thermal load of the passive cladding, and optimizing the sample geometry increased the cooling achieved by a factor of three for pumping with 20 W of 1035 nm light in-vacuum. In particular, a large core diameter was chosen to improve cooling, as the anti-Stokes fluorescence (extracted heat) is directly proportional to the Yb-doped core area. Record cooling was also observed under ambient pressure conditions for a different sample. Laser cooling to more than 6 K below room temperature was achieved for sample B in-air by pumping with 185 W of 1033 nm light.

3 Measuring the external quantum efficiency

3.1 Background

The previous chapter introduced two sample sets of cooling grade ytterbium doped silica glasses (see Table 1). The samples had ytterbium ion concentrations in excess of $5 \cdot 10^{25}$ ions per m^3, surpassing the intrinsic critical quenching concentration of fused silica [39]. Therefore, it is of high interest to assess the external quantum efficiency, which must be near unity in order for the cooling presented in the last chapter to occur. Since the glasses are doped with aluminium, it is expected that the rare-earth solubility has been enhanced and in turn the critical quenching concentration will be greater than that for pure fused silica. To measure the external quantum efficiency, the Laser Induced Thermal Modulation Spectroscopy technique (LITMoS test) is employed.

3.2 Experimental

In characterizing the external quantum efficiency of the glasses, first, the emission spectra are recorded (Figure 16). A 940 nm diode laser is used as the excitation source and coupled into a fiber with an objective lens. A multi-mode fiber is placed on the side surface of the Yb-doped fiber to collect the fluorescence which is then sent to an optical spectrum analyzer. An average of 50 acquisitions at the highest sensitivity setting were taken.

Low-power (i.e. at least two orders of magnitude below saturation, which is between roughly 30 W and 300 W, depending on the wavelength) cooling/heating experiments were conducted in a manner similar as that outlined in the previous chapter. Experiments were done in high vacuum at 10^{-6} torr to eliminate convective heating by air. Conductive heating was minimized by supporting the samples on a custom support consisting of a pair of crisscrossed 250 micron diameter fibers. Laser light
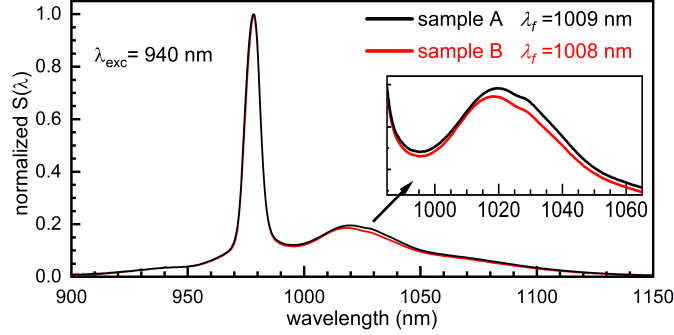
Figure 16: Emission spectra recorded with optical spectrum analyzer after excitation with 940 nm diode laser.

is coupled into the fiber through the vacuum chamber window using a 10 cm focal length AR coated lens. The temperature of the fiber is then monitored without contact using a thermal camera acquiring at 30 frames per minute. The thermal camera images are later analyzed to evaluate the temperature versus time relationship.

For excitation sources, three different laser diodes were used in these experiments, two fixed wavelength diodes for trials below 1000 nm and one diode capable of being tuned between 1025-1038 nm. For the short wavelength trials at 940 nm and 975 nm, the absorption is high and so using the power available directly from the laser diode (20-60 mW) was sufficient. For longer wavelengths, the diode laser was coupled into a homemade forward pumped fiber amplifier constructed with off the shelf parts. The amplifier provided clean, stable output of approximately 1 W for all wavelengths.

3.3   Results and discussion

Since the coupling into the fiber might be sensitive to different wavelengths as well as disturbances of the free space optical elements employed, reproducibility experiments were carried out for each fiber (Figure 17). For simplicity, these initial investigations were carried out at 10^{-3} torr. Using 1 W of 1035 nm light, cooling experiments on a given fiber were repeated three times, without any adjustments made between trials. Then, two more trials were conducted with the coupling of the light into the fiber (eg.
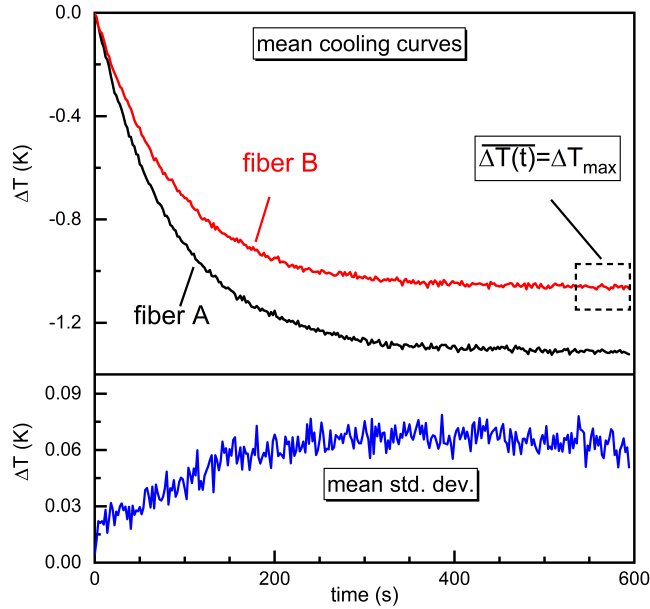
Figure 17: Average cooling curves for experiments pumping the fibers in-vacuum (10^{-3} torr) with $1\,\mathrm{W}$ of $1035\,\mathrm{nm}$ light (top) and the mean standard deviation (bottom). The top panel shows the average of the five consistency checks for fiber A (black) and fiber B (red). The standard deviations of the two lines in the top panel are averaged to give the mean standard deviation (bottom). To obtain ΔT_{max}, the ΔT over the indicated time interval is averaged.

launch angle, beam waist position) adjusted each time. Efficient coupling to the core of these large diameter fibers, and not into the cladding, can be qualitatively confirmed during alignment by holding an infrared detection card just beyond the output window of the vacuum chamber. From the five trials on each fiber, the standard deviation of $\Delta T(t)$ in the first 15 seconds was found to be $0.023\,\mathrm{K}$ for fiber A and $0.027\,\mathrm{K}$ for fiber B. The higher uncertainty in the less doped fiber B arises from the lower signal-to-noise ratio due to the lower cooling effect. The mean standard deviation after establishment of equilibrium was found to be $0.06\,\mathrm{K}$.

The primary figure of merit for the implementation of an optical cooling device is the cooling efficiency, η_c, which is defined as the ratio of the cooling power (P_{cool}) to the absorbed power (P_{abs}) so that $\eta_c = P_{cool}/P_{abs}$ [12]. Alternatively, the cooling efficiency may be expressed by Equation 7.

The mean fluorescence wavelength was determined with Eq. 2 from the min-max normalized emission spectra, $S(\lambda)$, shown in Figure 16 with the integration done over the interval 900 nm to 1200 nm. The spectra of Fig. 16 are nearly overlapping, except around 1030 nm, where sample A displays a higher relative intensity. This results in $\lambda_f^A = 1009$ nm compared to $\lambda_f^B = 1008$ nm, indicating that slightly more energy per pump photon is converted to fluorescence in sample B, but only a negligible 0.1% more. Alternatively, the increased intensity in the long wavelength regime of the more highly doped sample may actually be due to reabsorption of light in the 978 nm band.

To determine $\alpha_r(\lambda_p)$ for evaluation of η_{abs} (Equation 4), the cross sections are first calculated from the emission spectrum in Figure 16 using first the Füchtbauer-Ladenburg equation,

$$\sigma_{em}(\lambda, T) = \frac{\lambda^5}{8\pi n^2 c \tau(T)} \cdot \frac{S(\lambda, T)}{\int \lambda S(\lambda, T) d\lambda}, \tag{14}$$

where c is the speed of light, $n \approx 1.45$ is the refractive index of fused silica, and $\tau \approx 1$ ms is the spontaneous lifetime. From the emission cross section, the absorption cross section is calculated using McCumber theory [59]

$$\sigma_{abs}(\lambda) = \sigma_{em}(\lambda) \exp\left[\frac{hc}{\sigma_B T}\left(\frac{1}{\lambda} - \frac{1}{\lambda_o}\right)\right] \tag{15}$$

where h is Planck's constant, σ_B is the Boltzmann constant, T is the sample temperature, and λ_0 is the zero-line energy wavelength. From the absorption cross section, the resonant absorption coefficient spectrum is calculated by $\alpha_r(\lambda) = N_T * \sigma_{abs}(\lambda)$ where N_T is the Yb^{3+} ion dopant density. For both fibers, over the wavelength range studied, $\eta_{abs}(\lambda) \geq 0.998$ (Figure 18).

The cooling efficiency at each wavelength is determined using Equation 13. $\partial_t \Delta T|_{t=0}$ is determined experimentally by inspecting the thermal camera data at $t = 0$. The
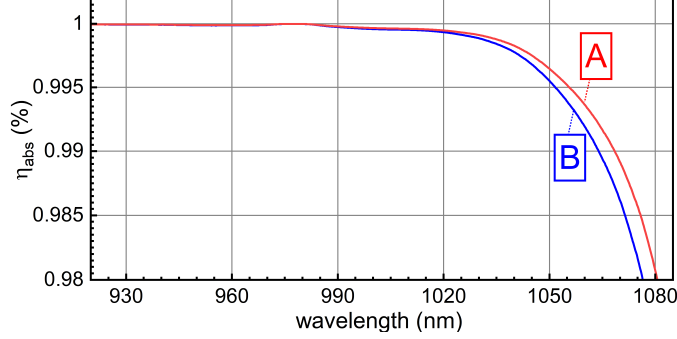
Figure 18: Absorption efficiency versus wavelength for sample A and sample B assuming $\alpha_b = 10\,\mathrm{dB} \cdot \mathrm{km}^{-1}$

.

error on this term comes from the standard deviation of $\Delta T(t)$ in the first 15 seconds as determined in the reproducibility studies (Figure 17). The absorbed power, P_{abs}, is calculated with the Beer-Lambert law for each trial via Equation 12. The error on P_{abs} comes from uncertainty in the $\alpha_r(\lambda_p)$ arising from the finite laser linewidth. With $\partial_t \Delta T|_{t=0}$ and P_{abs} determined, Eq. 13 can be evaluated to produce the scatter points presented in Figure 19.

The contents of Eq. 7 can then be rearranged to solve for η_{ext}. The quantum efficiency describes the capacity of a system to relax to the ground state through radiative decay channels as opposed to non-radiative decay channels that are accompanied by heating of the system (see [39] for a detailed discussion pertinent to the Yb:silica system). The average of all the trials gives $\eta_{ext}^A = 0.989$ and $\eta_{ext}^B = 0.991$. It is noted that considering only the data in the cooling regime, the η_{ext} values are slightly lower with $\eta_{ext}^A = 0.988$ and $\eta_{ext}^B = 0.989$

With values for η_{ext} in hand, Eq. 7 can be evaluated to give the theoretical cooling efficiency as a function of wavelength. This is displayed for each sample in Figure 19 as a solid black line. The apparently linear behavior is because $\alpha_r(\lambda_p) >> \alpha_b$ in the wavelength region investigated. At longer wavelengths, the resonant absorption decreases which results in $\eta_{abs}(\lambda_p)$ being increasingly dependent on the background absorption, causing the cooling efficiency to decrease and eventually switch signs [9].
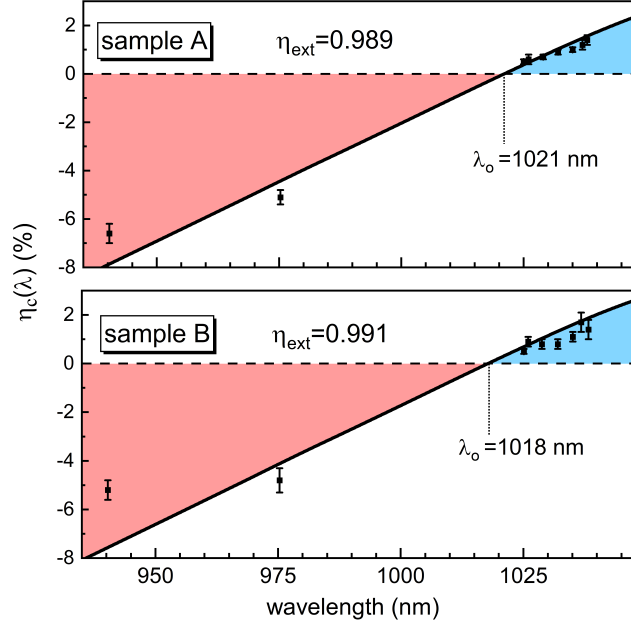
Figure 19: Wavelength dependent cooling efficiency for sample A (top) and sample B (bottom). Scatter points are experimentally measured values. Solid black lines represent theoretical cooling efficiency according to Eq. 7

.

For sample A, the theoretical value for $\eta_c(1035\,\text{nm}) = 1.3\%$ which is in excellent agreement with the value reported in the previous chapter. There, the power cooling experiments (using a different rod from the same draw) at $1035\,\text{nm}$ in-vacuum gave $\eta_c(1035\,\text{nm}) = 1.2 \pm 0.1\%$. It is also noted that the composition of sample B was studied previously in the state of a preform [9] and η_{ext} was reported to be 0.993, close in value to the external quantum efficiency obtained here from the drawn rod. This indicates that η_{ext} is not significantly impacted by the fiber drawing process suggesting that composition optimization studies for fiber laser cooling applications may be conducted on bulk glasses, a more convenient route to determine the most suitable concentration of co-dopants. Moreover, the in-house made glasses (at the Fraunhofer Institute for Applied Optics and Precision Engineering), display external quantum efficiency values on par with that of a commercial fiber investigated in [60] while the samples here contain more than 16 times the Yb^{3+} concentration.

Resolving Eq. 7 gives the so-called crossover wavelength, λ_0, which is important for designing a laser utilizing heat mitigation by ASF [7]. While the ideal condition for optical refrigeration is that $\lambda_p > \lambda_f$, the efficiency factors effect how this will actually play out in the laboratory. The crossover wavelength is then the true condition for laser cooling, $\lambda_p > \lambda_0$. Graphical inspection of Fig. 19 shows that $\lambda_0^A = 1021$ nm and $\lambda_0^B = 1018$ nm. This, along with the other stronger figures of merit for sample B (η_{ext}, λ_f) might be due to the higher Al:Yb ratio, which is favorable for efficient radiative relaxation as seen also by Knall et al. [43].

In addition to knowing λ_0, another design parameter of interest is undoubtedly the optimal wavelength at which to pump the sample. Focusing on the cooling regime, the ΔT_{max} normalized by the P_{in} of that trial is presented in Figure 20. The wavelength range with the best cooling performance per watt of input lies between 1032-1035 nm. This is in good agreement with the theoretical conclusion of 1035 nm being the optimal pump wavelength, derived from the relation $\Delta T \propto -\alpha(\lambda_p)\eta_c(\lambda_p)$ in Refs. [9, 42]. This expression captures the counteracting effects of the increasing $\eta_c(\lambda_p)$ and decreasing $\alpha_r(\lambda_p)$ with increasing λ_p. Theoretically considering the optimal pump wavelength for Yb:silica using the calculated absorption cross-section of sample A while varying η_{ext} values between 0.96 and 1 with α_b values between 1 and 20 dB km^{-1}, the optimal pump wavelength is independent of α_b over the range of values considered. For $\eta_{ext} = 1$ the optimal pump wavelength is predicted to be about 1030 nm and this shifts to longer wavelengths with decreasing η_{ext} (i.e. 1040 nm for $\eta_{ext} = 0.98$).

3.4   Conclusion

The results suggest that in addition to ultra-stable laser operating in the low-power regime [27, 26], ASF may be used to mitigate heat in high power lasers if unconventional doping schemes are utilized that leverage the cladding. Unconventional doping schemes have been utilized to achieve different objectives recently, such as saturable
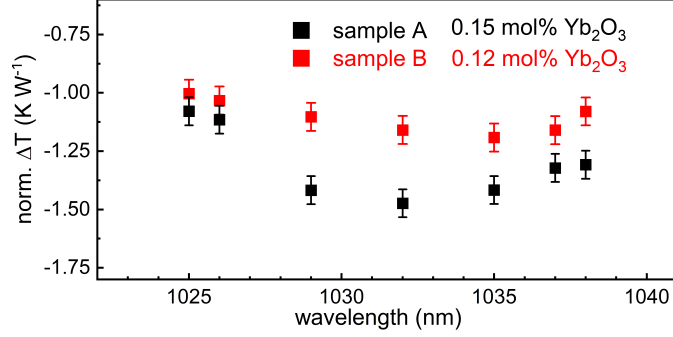
Figure 20: Maximum temperature difference achieved in high vacuum (10^{-6} torr) normalized to the input pump power indicating the optimal cooling wavelength region. The error bars are based on the reproducibility experiment (see Fig. 17)

.

absorbers [61] and high-power short wavelength Yb fiber lasers [62].

In this chapter, near unity external quantum efficiency values of in-house made glasses were measured while maintaining high Yb^{3+} ion densities suitable for power cooling experiments. In conjunction with previous work ([9]) this indicates that η_{ext} is not substantially altered by the fiber draw process. While it is expected that this will hold true for high core-cladding or doped-cladding fibers, it is possible that some of the properties, including η_{ext}, might be modified when drawn to small, single mode diameters. The crossover wavelength beyond which cooling by ASF is possible is 1018-1021 nm while the optimal pump wavelength for ASF cooling of these compositions lies between 1032-1035 nm.

4 Potential of ytterbium doped silica glass for solid-state optical refrigeration to below 200 K

4.1 Background

In the last chapter, high external quantum efficiencies were measured for both compositions outlined in Table 1. Several questions still remain. In Chapter 2, the in-vacuum trials carried out at UNM were limited to the available 20 W of pump power. On the other hand, colleagues in Jena saw cooling with up to around 185 W of pump power. This means that it is neccesary to bridge this gap. That is, to conduct in-vacuum cooling experiments with increased pump power. Towards this goal, a new mulit-stage fiber amplifier was constructed for this purpose and used in experiments. Another question present at this time is, how much can these samples be cooled? To address this second question, a temperature-dependent spectroscopic study is carried out to predict the temperature dependence of the cooling efficiency.

4.2 Results and Discussion

4.2.1 Laser cooling of Yb:silica to 255 K

The previous chapters discussed power cooling results [63] and external quantum efficiency measurements [64] of ytterbium doped silica glasses that have been manufactured by the modified chemical vapor deposition technique [45]. Chapter 4 concentrates on the more highly doped sample A. In Chapter 3, sample A displayed about the same external quantum efficiency (η_{ext} = 0.99) as sample B, but performed better in terms of cooling at a given pump power level. As described before but reviewed once more here, the sample is cylindrical with a doped core region of diameter $900\,\mu$m surrounded by a thin passive cladding $50\,\mu$m thick [65]. The core has a Yb^{3+} ion density of $6.56 \cdot 10^{25}$ ions per cubic meter (0.15 mol% Yb_2O_3). Aluminum

is present to increase the ytterbium solubility within the silicate framework [56, 57], with an Al:Yb ratio of 6:1. Fluorine was also added to the core to decrease the refractive index relative to the cladding [66]. The targeted and real numerical aperture of the core-cladding is 0.06, as measured on the preform with a commercial instrument. These materials were optimized for high power fiber-laser applications [31, 30]. This required fabrication of glasses with low background loss, high purity, low photodarkening, and careful attention to the doping profile. Optimization of such properties render these materials a perfect candidate for optical refrigeration.

The experimental setup is similar to that which used in the past [9, 42, 63], with some optimization and enhancement. A custom-built multi-stage fiber amplifier, constructed with off-the-shelf parts, provides up to 50 W of output. The seed consists of two fiber Bragg grating (FBG) lasers combined with a 2-to-1 coupler. The FBGs have center wavelengths 200 pm apart, 500 pm bandwidths, and 50% transmission at the respective center wavelengths. This resulted in laser emission at 1030 nm with a bandwidth of roughly 120 pm. A similar broadening approach was used in Reference [30]. The seed lasers are simultaneously pumped by the split output of a single mode 978 nm diode laser. The 5 cm long sample was placed on a fiber support system in a vacuum chamber held at about $1 \cdot 10^{-5}$ torr. These measures are taken to minimize the conductive and convective heat loads. Pump light was coupled into the sample through a 15 cm focal length anti-reflection (AR) coated plano-convex lens placed before the entrance to the chamber. The entrance and exit windows of the vacuum chamber have AR coatings to both maximize the available pump light and minimize the scattered pump in the chamber. In an additional effort to minimize the scattered pump light, another AR coated lens was placed inside the chamber at the output end of the cylinder to collimate and remove unabsorbed pump from the chamber.

Temperature measurements are made utilizing the non-contact method of differ-

ential luminescence thermometry (DLT) [67, 68]. The fluorescence of the sample was monitored through a fused silica window with collection optics and a $600\,\mu$m core diameter multimode fiber feeding a CCD spectrometer. Experimental spectra were acquired once per second with a $100\,$ms integration time. For a high signal-to-noise ratio, we area normalize the measured fluorescence over the interval $\lambda \in \{900,1020\}\,$nm, avoiding the influence of scattered pump light. Then, the difference is taken relative to ambient temperature, or the first measurement at the start of the experiment. The relationship between the absolute area considered in the difference spectra recorded by the spectrometer and the sample temperature was determined in separate calibration experiments using a low power laser diode near the pump wavelength as the excitation source and the sample placed inside a temperature controllable liquid nitrogen cryostat. For the calibration (as well as the spectroscopy discussed below), a sample from the same preform draw was used with identical dimensions of the sample used in laser cooling experiments.

The time-temperature evolution of the sample pumped with $50\,$W of $1030\,$nm laser light is shown in Figure 21a. Figure 21b displays the difference spectra, $\Delta S(\lambda)$, relative to the measured spectrum at the start of the experiment at $t = 0$ for $t = 30\,$s and $t = 240\,$s. As the temperature drops, so does the resonant absorption at wavelengths in the vicinity of the pump wavelength. Since fluorescence power is directly proportional to absorbed power, as a sanity check of our results, we plot the integrated absolute value area of the difference spectra, S_{DLT}, against the integrated intensity of the as-measured photoluminescence spectra over the interval $\lambda \in \{900,1020\}\,$nm (Figure 21c). A nice linear relationship is observed. When the minimum temperature is reached in Figure 21a and the sample is held at $41\,$K below room temperature, the measured photoluminescence intensity and extracted S_{DLT} after data processing are stable.
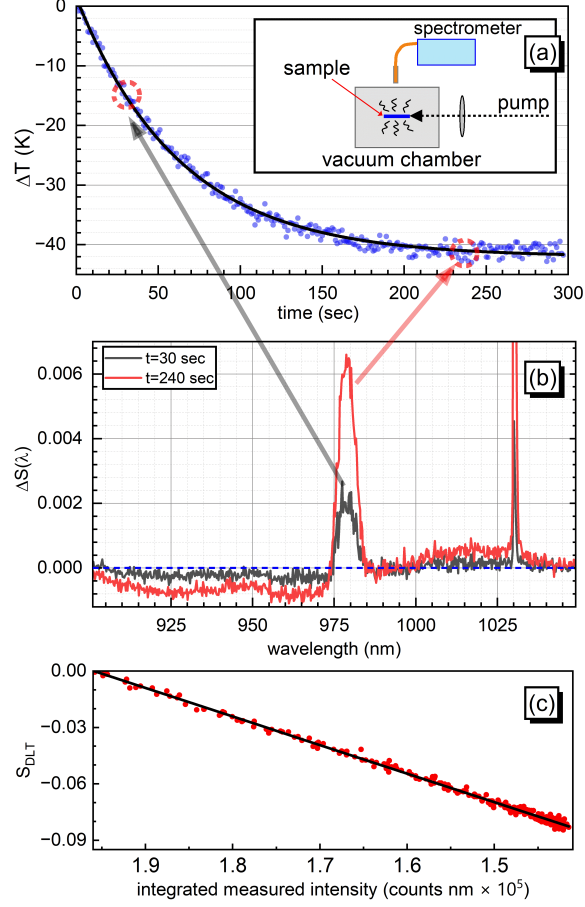
Figure 21: (a) Temperature versus time plot of an experiment with 50 W pump power at $\lambda_P = 1030\,\text{nm}$. The inset depicts the configuration of the experiment. (b) Difference spectra relative to $t = 0$ for $t = 30\,\text{s}$ and $t = 240\,\text{s}$ for the experiment shown in (a). (c) The integrated area of the DLT difference spectra as a function of the integrated intensity of the measured photoluminescence spectra over the duration of the experiment. In (a) and (b) the black lines are drawn to guide the eye.

4.2.2 Optical spectroscopy from 80 K to 400 K

In addition to these results, we report here an evaluation of the minimum achievable temperature (MAT) of cooling-grade ytterbium doped silica glass. To find the MAT, we need to evaluate the cooling efficiency given by Eq. 7 over a wide temperature range [69], i.e.,

35
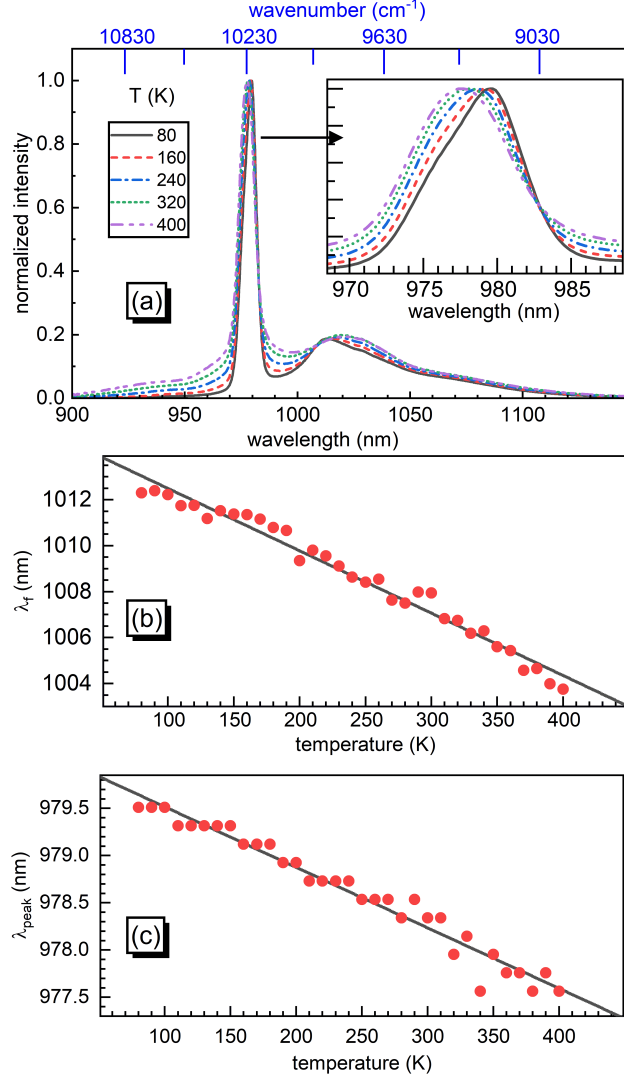
Figure 22: (a) Measured emission spectrum shown for selected temperatures. The inset highlights the shift to higher energies and broadening of the 978 nm transition. (b) Calculated mean fluorescence wavelength as a function of temperature. (c) Measured peak wavelength as a function of temperature.

$$\eta_c(\lambda_p, T) = \frac{\lambda_p}{\lambda_f(T)} \eta_{abs}(\lambda_p, T) \eta_{ext} - 1. \tag{16}$$

$\lambda_f(T)$ is calculated from steady-state fluorescence spectra (Figure 22a) [64]. The spontaneous emission spectra in Figure 22a were collected from the side of the previ-

ously mentioned calibration sample, using a 940 nm laser diode excitation source. The sample was mounted once again in the liquid nitrogen cryostat equipped with a heater. A 400 μm diameter fiber sent the collected light to an optical spectrum analyzer set at 1 nm resolution. As expected, the mean fluorescence wavelength increases with decreasing temperature. The mean fluorescence wavelength is fitted with a linear expression of $\lambda_f = b - mT$ where $b = 1015.2 \pm 0.2$ nm and $m = 0.0271 \pm 0.0008$ nm K^{-1}. It is interesting to note that this is very close to the slope of 0.03 nm K^{-1} that Seletskiy *et al.* found for ytterbium doped yttrium lithium fluoride (YLF) [69]. As can be seen in the inset of Figure 22a, the position of the peak at circa 977 nm broadens and shifts to shorter wavelengths as the temperature increases. This shift is shown in Figure 22c to be linear to a first-order approximation. The discretization is an artifact of the employed resolution of 1 nm of the optical spectrum analyzer, which was used to obtain measurements with good signal-to-noise ratio.
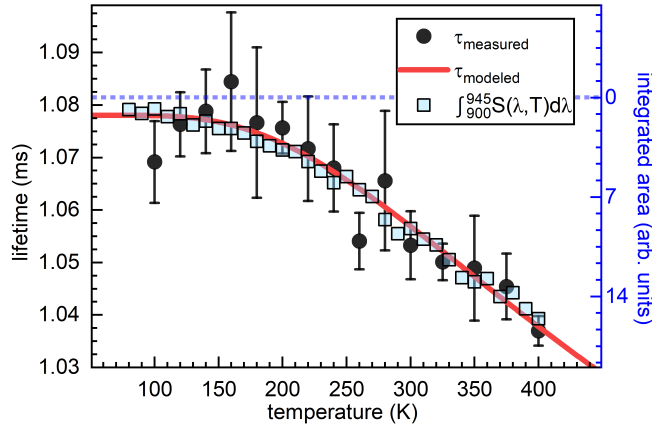
Figure 23: Depiction of the temperature dependence of the population of the second lowest sub-level in upper state manifold of Yb^{3+}. The measured lifetime as a function of temperature is shown by black circles. The solid red line was obtained by a two-level model fit of the measured lifetime data (Equation 17). The light blue squares represent the integrated area between $\lambda \in \{900,945\}$ nm in the steady-state fluorescence spectra. The axes have been scaled for comparison.

The radiative lifetime, τ_r, is required for computation of the emission cross-section. For high quantum efficiency materials, it is acceptable to make the approximation

$\tau_r \approx \tau_f$ where τ_f is the fluorescence lifetime. The τ_f values (see Figure 23, black circles) were measured using 978 nm single mode diode laser as the excitation source chopped to provide pulses of roughly 85 μs duration at a 95 Hz repetition rate. The chopped beam was focused into the sample in the cryostat. The fluorescence was collected and passed through a 1000 nm long pass filter toward an InGaAs amplified detector connected to an oscilloscope. A microscope slide was inserted into the path of the chopped beam so that the reflection was incident on a second detector to allow recording of the pulse shape and triggering the oscilloscope to allow acquisition in averaging mode. Measurements were repeated at each temperature with coupling into the sample lightly adjusted each time with the mirrors and lenses. The measured lifetimes are fitted with an expression for a two-level system [70],

$$\tau(T) = \frac{1 + \exp\left[-\delta E/k_B T\right]}{\tau_a^{-1} + \tau_b^{-1} \exp\left[-\delta E/k_B T\right]}, \tag{17}$$

where k_B is the Boltzmann constant, $\tau_{a(b)}$ is the lifetime of the first (second) energy level of the excited state, and δE is the energy difference between these two levels. The nonlinear fitting procedure gives $\tau_a = 1.078 \pm 0.003$ ms, $\tau_b = 0.79 \pm 0.09$ ms, and $\delta E = 597 \pm 129$ cm^{-1}. While the error of the fit is large on the value for $\delta E = 597$ cm^{-1}, it agrees well with the steady-state fluorescence data obtained in this study, as well as other reports [39, 71]. The observed lifetimes are a bit longer than those typically reported for Yb-doped silica optical fibers doped with fluorine and aluminum, which is typically around 0.8 ms [72, 73]. This is attributed to reabsorption effects due to the sample dimensions, both the diameter of the doped region and the length of the sample studied [6]. Similar reabsorption effects shift the measured mean fluorescence wavelength to longer values than the intrinsic value that can be measured in a small sample with negligible reabsorption [74]. However, in the characterization of

the MAT for a sample, it is preferred to use the observed values since the interactions yielding them (i.e. reabsorption, fluorescence trapping) will also be present in laser cooling experiments involving the studied sample [69]. As a result, we use the observed values in the calculations of our cross-sections.

Alternatively, insight into the distribution between the sub-levels in the upper manifold can also be determined from the steady-state fluorescence spectra. Equation 17 describes the distribution between the two lower levels of the upper manifold where a is the lowest level and b is the second lowest level. The lowest level is identified from the emission spectra 22a to be at $10230\,\mathrm{cm}^{-1}$ (taking the mean value of the two observed components). The fit of the observed lifetimes gives $\delta E \approx 600\,\mathrm{cm}^{-1}$, implying level b lies $600\,\mathrm{cm}^{-1}$ above a. This puts level b at circa $923\,\mathrm{nm}$. Insight into the wavelength range characteristic of this transition is acquired by inspecting the difference spectra in the cooling experiments (Figure 21b). As a reasonable approximation, the area between 900-945 nm is taken as representative of the population in b. Integrating this area of the normalized emission spectra (Figure 22a) and plotting against the temperature (see Figure 23, blue squares) produces almost the same trend as seen from the time-domain fluorescence measurements. Indeed, the integrated area and modeled $\tau(T)$ (Figure 23, solid red line) are linearly correlated with an R^2 value of 0.997.
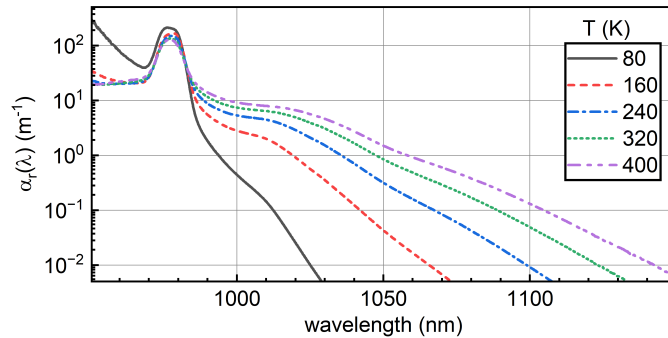
Figure 24: Calculated resonant absorption spectra shown at selected temperatures.

The $\eta_{abs}(\lambda_p, T)$ term requires knowledge of the resonant absorption spectrum as a

39

function of temperature. To obtain this, the Füchtbauer-Ladenburg equation (Equation 14) is applied to the measured emission spectra at different temperatures using $\tau(T)$ from the two-level model fit as the radiative lifetime at each temperature [75]. With the calculated emission cross-section, McCumber theory allows the determination of the absorption cross section (Equation 15) [59]. This in turn allows us to obtain $\alpha_r(\lambda, T)$ by scaling with the Yb^{3+} ion dopant density via $\alpha_r(\lambda, T) = \sigma_{abs}(\lambda, T) * N_T$. $\alpha_r(\lambda, T)$ is shown in Figure 24 for selected temperatures.

4.2.3 The minimum achievable temperature

With the results of our spectroscopic measurements and taking $\alpha_b = 10\,\text{dB·km}^{-1}$ [9], we can fully evaluate $\eta_c(\lambda_p, T)$, which is shown in Figure 25. We employ here the convention of a positive cooling efficiency coinciding with cooling, and so the blue region encompasses the cooling window. To determine the MAT$_G$, we graphically inspect the white contour in Figure 25 where $\eta_c(\lambda_p, T) = 0$, which represents the minimum achievable temperature spectrum, MAT(λ). At a given wavelength, the temperature corresponding to $\eta_c(\lambda_p, T) = 0$ gives the local MAT, and solid-state cooling is no longer possible at that wavelength at lower temperatures. MAT$_G$ is then given by the lowest temperature at which $\eta_c(\lambda_p, T) = 0$. The MAT$_G$ of the sample under investigation is found to be 151 K (Figure 25). For simplicity, we assume in this analysis that η_{ext} and α_b are temperature independent [69, 76]. Before solid-state cooling of Yb:silica was ever observed, a spectroscopic investigation by Mobini *et al.* was conducted using a commercial ytterbium doped silica single mode optical fiber [39]. Based off their measurements and assumptions, they predicted the MAT of Yb:silica to be 175 K with an assumed $\eta_{ext} = 0.99$. This was already a lower MAT than determined for ZBLAN, which is about 190 K [69].

The measurements reported here are on our in-house (Fraunhofer IOF, Jena, Germany) made glasses, for which we have experimentally measured an $\eta_{ext} = 0.99$ and
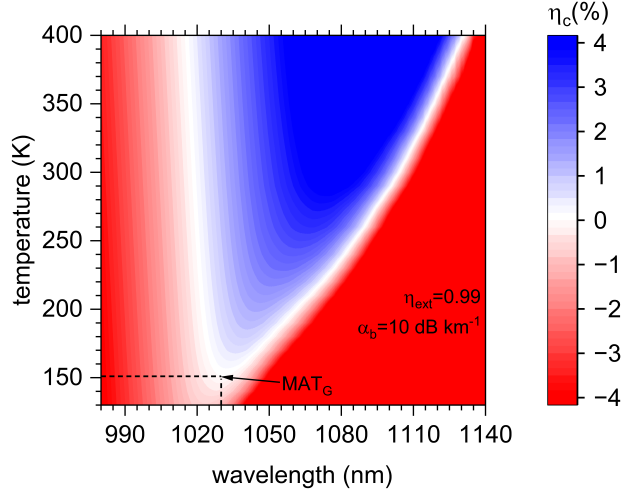
Figure 25: Cooling efficiency versus wavelength and temperature.

repeatedly shown cooling (see Chapter 2 and Chapter 3) [63, 64], indicate the MAT is about 24 K below what was previously thought possible for ytterbium doped silica. Moreover, this direct calculation on a true cooling-grade sample shows that Yb:silica can be optically cooled below temperatures presently achieved by off-the-shelf thermo-electric coolers. While this is not as low as the MAT of some fluoride crystals [77], silica has some advantages such as being rugged, isotropic, and able to be readily formed into microspheres, planar substrates, and drawn into fibers.

Considering our decision to use the observed $\tau(T)$ relation, we compute the MAT_G for values of τ that are more characteristic of the typically found intrinsic lifetime of Yb^{3+} in silica. These produce lower MAT_G values. For example, setting $\tau = 0.85\,\mathrm{ms}$ gives $\mathrm{MAT}_G = 144\,\mathrm{K}$. As such, we are satisfied with our more conservative calculation employing the extrinsic values relevant to our experiments and sample.

4.2.4 Potentially better potential?

A recent study by Volpi *et al.* revealed that the background absorption decreased significantly in a Yb:YLF specimen with decreasing temperature [44]. In addition, the α_b of rare-earth doped silica fibers can in some cases be as small as 3-5 dB·km^{-1} [9]. Pas-
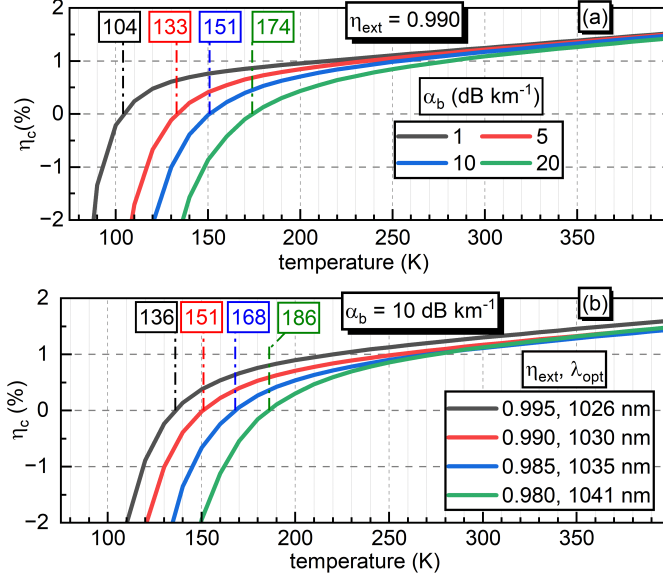
Figure 26: Cooling efficiency versus temperature for (a) several background absorption values with fixed external quantum efficiency and (b) several external quantum efficiency values with fixed background absorption.

sive fibers used by the telecommunications industry routinely display $\alpha_b < 1\,\mathrm{dB\cdot km^{-1}}$, but this is not attained in rare-earth doped fibers despite using modern methods. In light of this, we fix the pump wavelength at $\lambda_p = 1030\,\mathrm{nm}$ and take $\eta_{ext} = 0.99$ then consider several different values of α_b that might be accessible (Figure 26a). The calculation indicates that lower MATs might be achievable in ytterbium doped silica, possibly below cryogenic levels.

The importance of the background absorption at low temperature in Yb-doped silica is highlighted in Figure 26b. We've taken a fixed, rather standard, value for silica fabricated by CVD of $10\,\mathrm{dB\cdot km^{-1}}$ and evaluated the cooling efficiency at different values of η_{ext} and the corresponding optimal pumping wavelength. Although an improvement in the external quantum efficiency will increase the cooling efficiency around room temperature, the background absorption demands more attention for future progress. Especially since α_b values between 3 and $5\,\mathrm{dB\cdot km^{-1}}$ have been reported, while an $\eta_{ext} = 0.995$ has not been achieved yet in Yb:silica, to our knowledge.

4.3   Conclusions

This chapter discussed the laser cooling of silica glass co-doped with ytterbium and aluminum by $41\,\mathrm{K}$ starting at room temperature. Then, temperature dependent spectroscopic measurements allowed the calculation of the minimum achievable temperature of this sample. The MAT was found to be in the vicinity of $150\,\mathrm{K}$ which is lower than the previously suggested MAT of $175\,\mathrm{K}$, as well as below the limit of typical thermo-electric coolers. Questions about the temperature dependence of the background absorption in Yb^{3+} doped silica glass remain.

5   Site-selective spectroscopy and its impact on laser cooling parameter characterization

5.1   Background

In order to optimize Yb:silica for cooling performance and facilitate comparison between the results of different research groups, proper characterization must be carried out. This shouldn't necessarily be complicated, as the spectroscopy of Yb^{3+} is generally quite straightforward (Figure 3). The ytterbium atom has an electronic configuration $[Xe]4f^{14}6s^2$. In oxide materials, the trivalent oxidation state is preferred and one f shell electron is sacrificed for the ionized configuration $[Xe]4f^{13}$. The one unpaired electron gives rise to just one ground and one excited state, $^2F_{7/2}$ and $^2F_{5/2}$, respectively. The degeneracy of these states is completely removed in amorphous materials, producing 3 sub-levels in the $^2F_{5/2}$ upper manifold and 4 sub-levels in the $^2F_{7/2}$ lower manifold.

More often than not, a two-level model is assumed for Yb:silica. In this conceptualization, after exciting a Yb^{3+} ion in thermal equilibrium in the lower manifold ($^2F_{7/2}$) to the upper manifold ($^2F_{5/2}$), the population in $^2F_{5/2}$ thermalizes on the or-

der of picoseconds to nanoseconds. Since the fluorescence lifetime of a Yb^{3+} ion is on the order of a millisecond, the much faster thermalization rate should make the distribution in the upper manifold at the time of decay independent of the energy that initially caused the excitation. As a direct result of this, the emission spectrum created by the ensemble of radiative decays from $^2F_{5/2} \rightarrow^2 F_{7/2}$ should be invariant at a given temperature.

This model can hold for broadband excitation sources; however, excitation by narrowband sources, such as a laser, can result in greater relative absorption by a subset of ions in a given coordination environment. The result is variations in the emission spectrum as a function of excitation wavelength due to the degree of participation in the optical process by different ions in different environments. The systematic investigation of this phenomenon is known as site-selective spectroscopy or fluorescence-line narrowing [78]. Eu^{3+} doped glasses have been particularly well-studied by these methods [79, 80, 81]. In the context of Yb^{3+} doped silica, Magne et al. observed dependence of the fluorescence lineshape on the excitation wavelength in a single-mode ytterbium doped silica fiber co-doped with phosphorous and germanium [82]. Later, Alimov et al. performed a detailed site-selective spectroscopic investigation using a commercial large-mode area Yb:silica fiber [83]. In addition to emission lineshape variation with changing excitation wavelength, fluorescence lifetimes of discrete emissions varied between 830 to 992 μs [83].

In this chapter, the excitation wavelength (λ_{exc}) dependence of the fluorescence behavior of ytterbium doped silica is studied at different temperatures using a cooling-grade Yb,Al co-doped silica rod. Parameters relevant to optical refrigeration are calculated. Then, the laser cooling performance is modeled with these quantities to demonstrate the dependence of both theoretical optimal pump wavelength and the minimum achievable temperature on what λ_{exc} is used in the laboratory measurements.

5.2 Experimental

A 1.2 cm long section of sample B (Table 1) was cleaved for spectroscopic measurements. The more lightly doped sample was used for this work to minimize reabsorption affects.

Temperature-dependent static fluorescence spectroscopy was carried out in a liquid nitrogen cryostat equipped with an electrical heater (See Figure 27). The chamber was held at approximately 10^{-5} torr for the duration of the experiment. The glass sample was clamped against a copper cold finger. Fiber coupled butterfly laser diodes were used as excitation sources. Perpendicular to the length of the rod, collection optics located outside of the cryostat chamber coupled the fluorescence into a 400 μm core diameter step-index multimode fiber. An optical spectrum analyzer was then used to record the fluorescence. Spectra were collected at high sensitivity with a 1 nm resolution. Scattered laser light in the measured spectrum was removed and replaced by interpolated values. The temperature step size between measurements was 10 K.

Time-domain fluorescence decay measurements were made at room temperature by incorporating a mechanical chopper into the experimental setup. A microscope slide was inserted into the beam path after the chopper to reflect a fraction of the excitation pulse toward a Si photodetector to monitor the pulse width ($37 \pm 5\mu$s) and trigger acquisition of the fluorescence signal. The modulated fluorescence was collected with the same arrangement as for the steady-state measurements, but with the output of the multimode fiber coupled to an InGaAs photodetector. Both photodetectors were connected to a two-channel 350 MHz oscilloscope. For excitation wavelengths less than or equal to 940 nm, a 950 nm long pass filter was used. 977 nm and 1030 nm excitations used a 980 nm notch filter and a 1000 nm short pass filter, respectively.
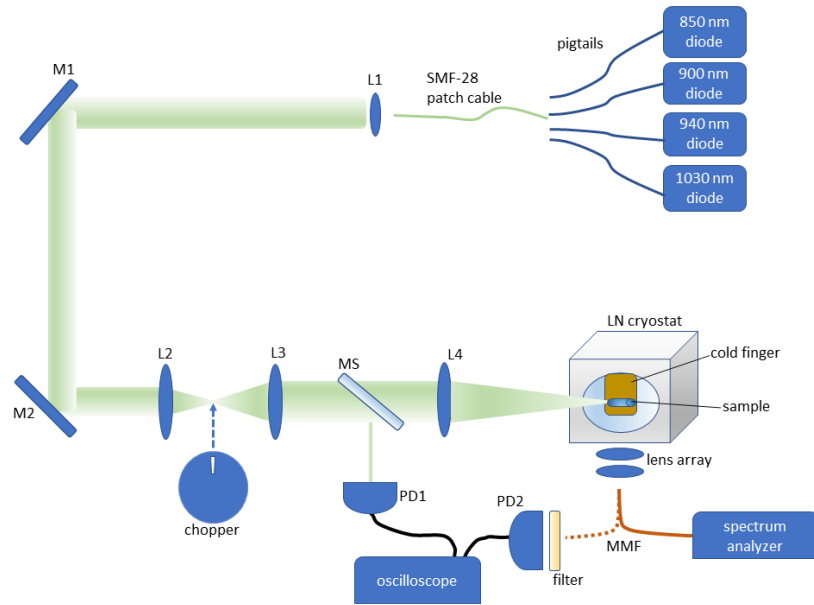
Figure 27: Schematic of experimental setup including pigtailed laser diodes, SMF-28 patch cable to connect to diode pigtails, collimating lens (L1), and steering mirrors (M1, M2). A pair of lenses (L2, L3) was used to focus and recollimate the beam. For lifetime measurements, a chopper was inserted at the focus spot. Light was coupled into the sample with a lens (L4) and a lens array outside the chamber coupled the fluorescence into a multimode fiber (MMF). For spectral measurements, the MMF connected to a spectrum analyzer. For lifetime measurements, the output of the MMF was filtered (see main text) and incident on a photodetector (PD2). A microscope slide (MS) sent a fraction of the beam to a different photodetector (PD1) for triggering PD2 on the oscilloscope.

5.3 Results and discussion

The dependence on excitation wavelength (λ_{exc}) is most pronounced by viewing the low temperature (80 K) fluorescence in Figure 28. The intensity on the ordinate axis is plotted in a logarithmic scale (base 10) to aid in the visualization of the 990-1140 nm envelope. The spectrum at 80 K under 850 nm excitation is broad and diffuse, lacking distinct features. As λ_{exc} increases from 850 nm to 935 nm, the prominent high energy band from $E_5 \rightarrow E_1$ transitions shifts from 977 nm to around 980 nm. This band is the so-called "zero-phonon line" (ZPL) transition. Lower energy excitation produces increasingly varied emission in the long wavelength regime. The envelope spanning 990-1140 nm displays the opposite trend of the ZPL, with the average emission shifting to higher energies with decreasing excitation energy. Attention is drawn in Figure 28 via vertically oriented dashed lines to the variation in the relative intensity of features at 1016 and 1036 nm. Increasing λ_{exc} from 905 nm to 935 nm results in a decrease in the relative intensity at 1036 nm and the growth of spectral intensity at 1016 nm. This trend coincides with the long wavelength tail falling to 1% of the maximum intensity value at shorter wavelengths. When $\lambda_{exc} < 915$ nm this cut-off is seen at about 1130 nm whereas for $\lambda_{exc}=935$ nm the 1% cut-off occurs at about 1115 nm. Overall, these trends signal a lower Stark splitting of the $^2F_{7/2}$ manifold associated with sites probed by lower excitation energy.

The ZPL bands in Figure 28 were seen to be highly asymmetric, particularly at $\lambda_{exc} \geq 920$ nm. These features were fit with Voigt component bands in OriginLab. The measured spectra, simulated spectra, fit residuals, and component bands are shown for different λ_{exc} in Figure 29. In all instances, 2 components adequately describe this spectral feature. This nature of the ZPL band has not been reported before in site-selective excitation studies of ytterbium doped silica [82, 83]. The modeling of the $E_5 \rightarrow E_1$ as two components is convincing. The most plausible explanation at this time seems to be that the ytterbium ions exist in two (or more) non-equivalent
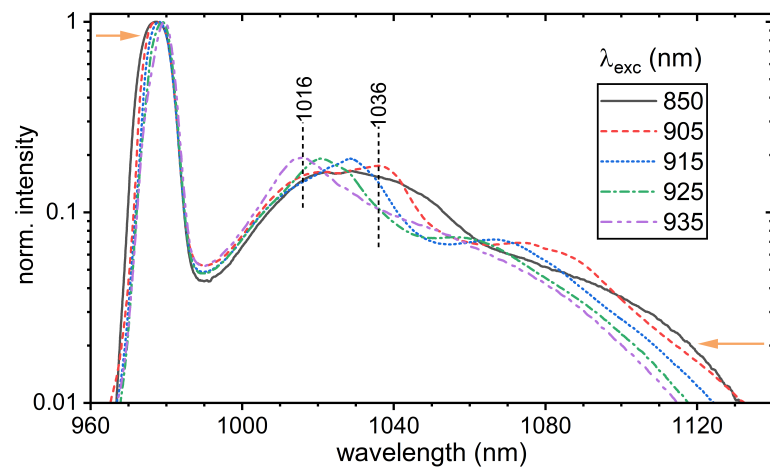
Figure 28: Normalized emission spectra at 80 K shown with logarithmic intensity scale.
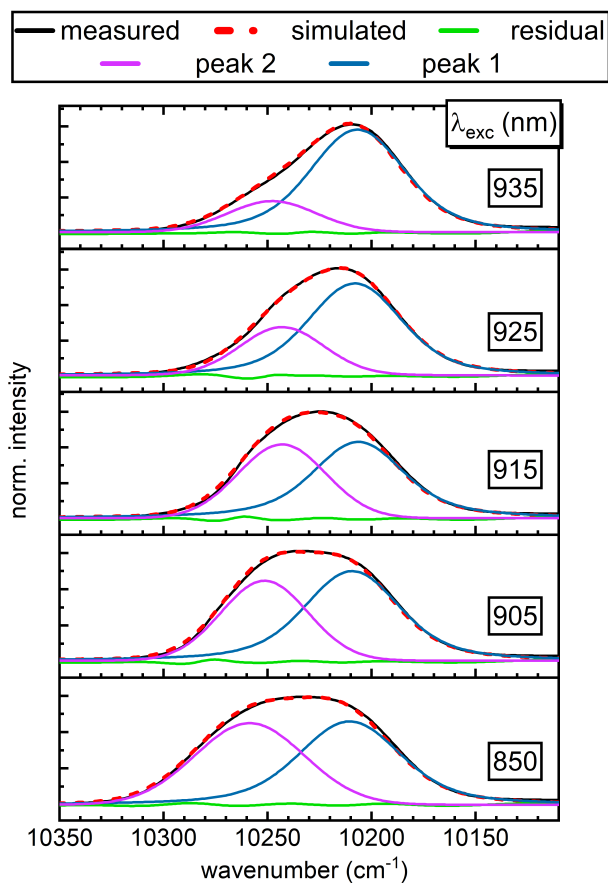
Figure 29: Decomposition of zero-phonon line transition at 80 K into two Voigt bands.

48

Table 3: Comparison of zero-phonon line transitions as identified by band fitting here (See Figure 29) with crystalline materials characterized by two distinct sites.

	Host	Site 1 (cm^{-1})	Site 2 (cm^{-1})	$\Delta\nu$ (cm^{-1})
This work ($\lambda_{exc} = 850$ nm)	Al,F:SiO_2 (glass)	10211	10258	47
This work ($\lambda_{exc} = 905$ nm)	Al,F:SiO_2 (glass)	10209	10250	41
This work ($\lambda_{exc} = 915$ nm)	Al,F:SiO_2 (glass)	10206	10242	36
This work ($\lambda_{exc} = 925$ nm)	Al,F:SiO_2 (glass)	10208	10242	34
This work ($\lambda_{exc} = 935$ nm)	Al,F:SiO_2 (glass)	10207	10247	40
Ref [84, 85]	Y_2SiO_5	10189	10216	27
Ref [85]	Lu_2SiO_5	10189	10214	25
Ref [85]	Sc_2SiO_5	10196	10219	23
Ref [86]	$SrSc_2O_4$	10249	10281	32
Ref [86]	$CaSc_2O_4$	10247	10291	44

environments within the aluminosilicate matrix. Such is the case for some Yb^{3+} doped rare-earth orthosilicate crystals and alkaline-earth scandate crystals, in which the rare-earth ion constituents occupy two distinct crystallographic sites, either of which the Yb^{3+} dopant can substitute into. The coordination environments differ between sites, resulting in differences between the crystal field acting on an ion in one site versus the other. This then produces Stark levels at different energies for each site. The energies of the $E_5 \rightarrow E_1$ transition of Yb^{3+} in different crystalline hosts is compared to the separation between the fitted components here in Table 3. At 80 K, the mean separation between the component band centers is 40 ± 5 cm^{-1}, which is greater than in crystalline rare-earth orthosilicates but comparable to alkaline-earth scandates [84, 85, 86].

To investigate how this site-selective behavior influences characterization of laser cooling parameters, we selected four wavelengths to measure the temperature-dependence of the emission lineshape. λ_{exc}=850 nm was selected as it lies in the blue tail of the $E_1 \rightarrow E_7$ absorption band and has no overlap with the emission spectrum. λ_{exc}=900 nm was selected as it lies just outside the emission spectrum at room temperature and below, but the absorption is much greater than that at 850 nm, so a strong emission spectrum can be measured with less incident power. λ_{exc}=937 nm
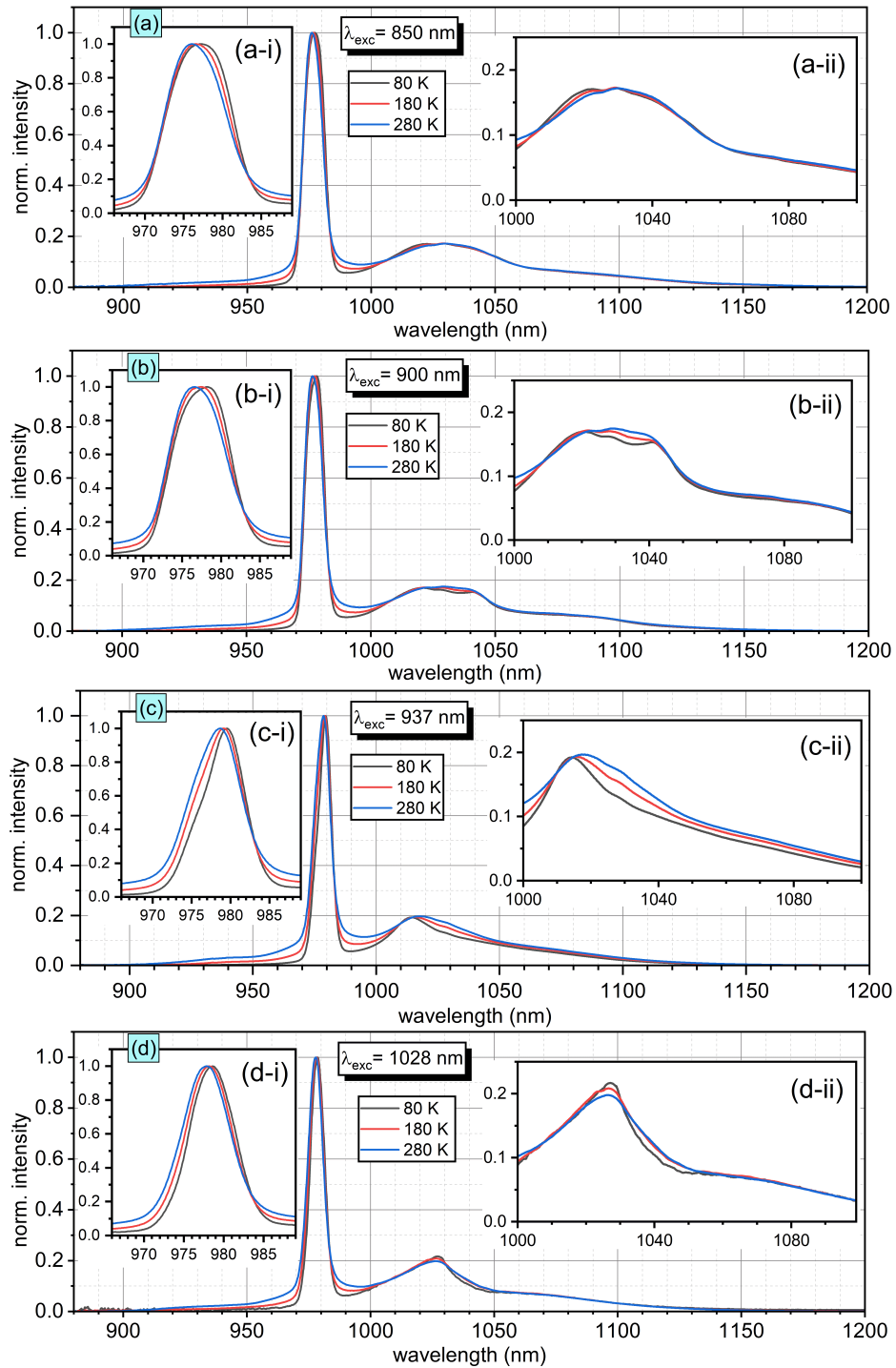
Figure 30: Normalized emission spectra at 80, 180, and 280 K for different excitation wavelengths.
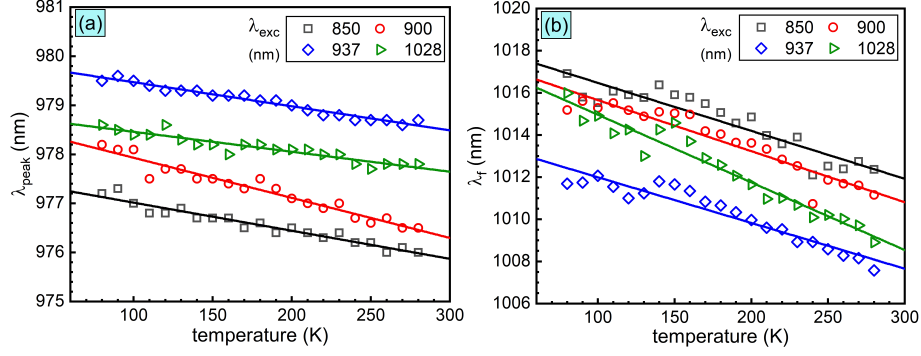
Figure 31: (a) Temperature dependence of the peak wavelength for different excitation wavelengths. (b) Temperature dependence of the the mean fluorescence wavelength for different excitation wavelengths. All straight lines represent linear fits of the data.

was selected as this is approximately what we have used previously in characterization of our samples [64, 87]. λ_{exc}=1028 nm was selected because it lies well beyond the mean fluorescence wavelength and cooling has been demonstrated in this wavelength regime. The emission spectra at 80, 180, and 280 K are shown in Figure 30 for excitation at 850, 900, 937, and 1028 nm. The insets on the left side of each panel highlight the ZPL transition. For all λ_{exc}, the wavelength at which the maximum intensity of this peak occurs (λ_{peak}) increases with decreasing temperature in a linear manner (Figure 31a).

The insets on the right side of each panel in Figure 30 highlight $E_5 \rightarrow E_{4,3,2}$ transitions. In the region between 1010-1045 nm, only two components are expected, corresponding to the $E_5 \rightarrow E_2$ and $E_5 \rightarrow E_3$ transitions. However, clearly for λ_{exc}=900 nm (and to some extent in λ_{exc}=850 and 937 nm) this region displays features at roughly 1021, 1028, and 1040 nm. This occurrence seems to support the notion of two main local environments of Yb^{3+} ions. Unfortunately the broad bands are not individually resolved, as is typical for glasses [88], and two distinct Stark manifolds cannot be unambiguously determined.

Our main goal is to determine how the excitation dependence of the fluorescence spectra as seen in Figure 30 impacts characterization of the material in the context

51

of laser cooling. To achieve net cooling in a rare-earth doped material, the system is pumped at λ_p in the red-tail of the absorption spectrum beyond the mean fluorescence wavelength, λ_f. In this way, the average emitted photon is blue-shifted relative to the absorbed pump photon permitting the fluorescence to successfully extract heat from the system. The cooling efficiency, η_c, of an optical refrigerator can be written, for the ideal case, as $\eta_c(\lambda_p, T) = \frac{\lambda_p}{\lambda_f(T)} - 1$ (the temperature dependent form of Equation 3). The results in Figure 30 show that $S(\lambda, T) \rightarrow S(\lambda, T; \lambda_{\mathrm{exc}})$. This then requires Equation 2 to be adjusted accordingly,

$$\lambda_f(T; \lambda_{\mathrm{exc}}) = \frac{\int \lambda\, S(\lambda, T; \lambda_{\mathrm{exc}})\, d\lambda}{\int S(\lambda, T; \lambda_{\mathrm{exc}})\, d\lambda}. \tag{18}$$

The temperature dependence of λ_f for different excitation wavelengths is shown in Figure 31b. The solid lines represent linear fits of the data, $\lambda_f(T) = b - mT$ [87, 69]. Considering the variation in the mean fluorescence wavelength, we take a moment to revisit our previous results. In Chapter 3, the Laser Induced Thermal Modulation Spectroscopy (LITMoS) method was used to measure η_{ext} of a sample from the same preform as this sample. The mean fluorescence wavelength was measured using 940 nm excitation, before we were aware of the dependence of $S(\lambda, T)$ on λ_{exc}. At the time λ_f=1008 nm was found, which agrees very well with what is found here for λ_{exc}=937 nm at room temperature. Measurements here however show that when excited at longer wavelength around 1030 nm, λ_f is slightly longer. Thus our previous measurements represent a slight underestimation of η_{ext}. For the current sample, this is mostly negligible, as we find that an increase in λ_f by 1 nm raises the obtained η_{ext} value by $\approx 0.1\%$. However, it is recommended that in future LITMoS tests on materials exhibiting site-selective behavior, that the λ_f is recorded at each experimentally used wavelength.

With Equation 18, it is clear that modeling of the ideal cooling efficiency, for the case of a material for which the emission has a dependence on the excitation wavelength, turns into a function of how one goes about measuring the system at hand and the temperature dependent form of Equation 3 then turns into

$$\eta_c(\lambda_p, T; \lambda_{\mathrm{exc}}) = \frac{\lambda_p}{\lambda_f(T; \lambda_{\mathrm{exc}})} - 1. \tag{19}$$

As discussed in previous chapters, two efficiency terms are introduced into the cooling efficiency model, η_{ext} and η_{abs}. η_{ext} is the external quantum efficiency which describes how likely an incident photon is to subsequently undergo a radiative decay as opposed to a non-radiative decay, which has no potential to extract heat. η_{abs} is the absorption efficiency and represents the likelihood of pump photons to be absorbed by the dopant species which has the capacity to extract heat rather than be lost to some parasitic background process that can induce heating. For cooling grade materials, the product $\eta_{\mathrm{ext}}\eta_{\mathrm{abs}}$ is typically required to be greater than 0.98. The cooling efficiency is then written with these considerations as

$$\eta_c(\lambda_p, T; \lambda_{\mathrm{exc}}) = \frac{\lambda_p}{\lambda_f(T; \lambda_{\mathrm{exc}})}\eta_{\mathrm{ext}}\eta_{\mathrm{abs}}(\lambda_p, T; \lambda_{\mathrm{exc}}) - 1. \tag{20}$$

The absorption efficiency term in Equation 20 is written as function of the pump wavelength, the temperature, and how the measurements were performed. To see this clearly, we must take a step back. The first quantity extracted from the emission lineshape is the emission cross-section, σ_{em}, using the Füchtbauer-Ladenburg equation (Equation 14) and accounting for the dependence on λ_{exc} [75, 39]

$$\sigma_{\mathrm{em}}(\lambda, T; \lambda_{\mathrm{exc}}) = \frac{\lambda^5}{8\pi n^2 c\tau} \cdot \frac{S(\lambda, T; \lambda_{\mathrm{exc}})}{\int \lambda S(\lambda, T; \lambda_{\mathrm{exc}})d\lambda}, \tag{21}$$
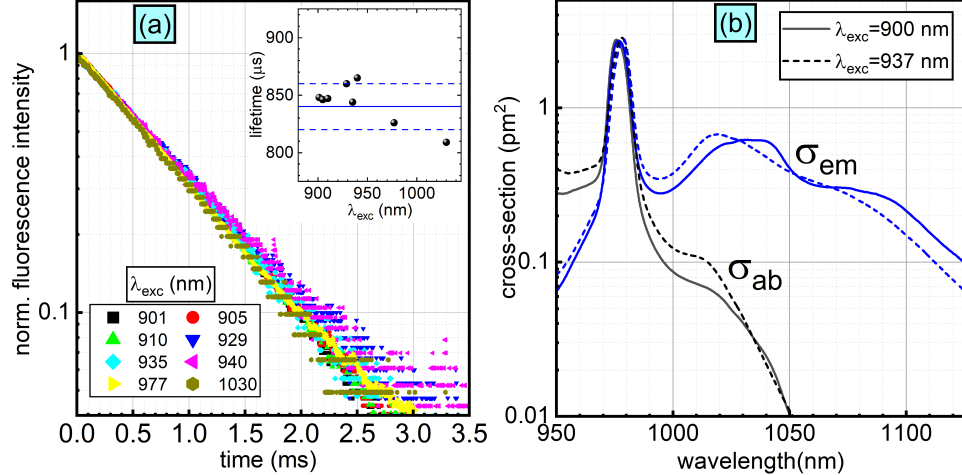
Figure 32: (a) Fluorescence decay curves measured for different excitation wavelengths measured at room temperature. (b) Absorption (black) and emission (blue) cross-sections for λ_{exc}=900 nm (solid) and λ_{exc}=937 nm (dashed) measured at 280 K

where c is the speed of light, $n \approx 1.45$ is the refractive index of fused silica, and τ is the spontaneous lifetime. Time-dependent fluorescence decays measured at room temperatures for several excitation wavelengths are shown in Figure 32a. The broadband detection approach used here did not detect systematic differences in lifetimes (see inset of Figure 32a). The mean lifetime for all excitation wavelengths was found to be 840±20 μs. The methods used here can not exclude the possibility that different emission transitions could have different lifetimes, as Alimov et al. observed [83]. Variation in local site environment often results in the measurement of different lifetimes [89], although recent work on terbium doped sodium borosilicates has seen identical lifetimes measured on bulk samples that displayed site variation of terbium ions when viewed with high resolution transmission electron microscopy [90]. At any rate, a value of τ=840 μs was employed in the calculations of the emission cross-sections using Eq. 21. In the previous chapter, it was shown that τ in Yb^{3+} doped silica increases by approximately 30 μs as temperature decreases from room temperature to liquid nitrogen temperature, as also reported by others, [71, 87]. The temperature dependence of τ is ignored here for simplicity.

As before, McCumber relations then permit the absorption cross-section, σ_{ab}, to be calculated from σ_{em} by [59]

$$\sigma_{\text{ab}}(\lambda, T; \lambda_{\text{exc}}) = \sigma_{\text{em}}(\lambda, T; \lambda_{\text{exc}}) \exp\left[\frac{hc}{\sigma_B T}\left(\frac{1}{\lambda} - \frac{1}{\lambda_{\text{peak}}}\right)\right], \qquad (22)$$

where h is Planck's constant, σ_B is the Boltzmann constant, and T is the sample temperature. λ_{peak} is officially supposed to be the ZPL wavelength but is instead taken here as the wavelength at which the maximum intensity is achieved in each measured spectrum. The calculated emission and absorption cross-sections are shown at $280\,\text{K}$ in Figure 32b for λ_{exc}=900 nm and λ_{exc}=937 nm. The laser physicist will immediately see that this discrepancy then leads to non-unique gain profiles. Measuring the absorption spectrum with a whitelight source and subsequently calculating the cross-sections seems like an obvious solution to remove the dependence of σ_{em} and σ_{ab} on λ_{exc}. However, this methodology leads to large errors in the long wavelength regime, where the absorption is low. This long wavelength regime is particularly important for the predictive modeling and optimization of lasers employing Bowman's radiation-balancing concept [28]. Bowman's proposition was that in an ultra-pure material, the anti-Stokes fluorescence could offset the heat generated by lasing [7, 23]. Recently, Knall and co-workers demonstrated radiation-balancing lasing and amplification in ytterbium doped silica fibers [26, 27]. Such schemes require pumping in the long wavelength regime, where the absorption is intrinsically low. Of course, direct absorption measurements at a specific laser wavelength can be made on fibers with the cut-back method, or, alternatively non-destructive techniques via side-light analysis [91, 34]. Unfortunately though, this limits the available data accessible for modeling and simulation. To resolve the emission cross-section dilemma, Figure 32 suggests that modeling and simulation should employ emission spectra acquired directly at λ_{exc} equal to the pump wavelength intended to be used.

Finally, our last task is to deal with the absorption efficiency factor (Equation 4). This requires the absorption coefficient spectrum, $\alpha_r(\lambda, T)$, which is given by the product of $\sigma_{\mathrm{ab}}(\lambda, T)$ and the ion dopant density, N_T. The absorption efficiency is then given by

$$\eta_{\mathrm{abs}}(\lambda_p, T; \lambda_{\mathrm{exc}}) = \frac{1}{1 + \dfrac{\alpha_b}{\alpha_r(\lambda_p, T; \lambda_{\mathrm{exc}})}}, \tag{23}$$

where α_b is the parasitic background absorption [44, 92, 93]. Evaluation of Equation 16 with directly measured quantities has become the standard approach for modeling the cooling efficiency for different pump wavelengths as temperature decreases [94, 69, 44]. By plotting Equation 16, one can find the contour where $\eta_c = 0$. This contour provides the MAT at which the material can be cooled with optical refrigeration at the particular pump wavelength. The lowest temperature on this contour is the global MAT (MAT_G) and occurs at the optimal pumping wavelength (λ_{opt}) for implementing solid-state laser cooling at low-temperature. However, at this point it is quite clear that in the presence of site-selective excitation, this approach will not give a singular MAT_G nor λ_{opt}. Taking the previously found $\eta_{\mathrm{ext}} = 0.99$ [64] for this sample and reasonably assuming $\alpha_b = 10\,\mathrm{dB \cdot km}^{-1}$ [9], Equation 20 is plotted for different excitation wavelengths in Figure 33

In Figure 33, the cooling efficiency contours are slightly different, reflecting the variation in the measured $S(\lambda, T)$ with different λ_{exc}. For this particular sample, the MAT_G varies from $151\,\mathrm{K}$ for $\lambda_{\mathrm{exc}} = 937\,\mathrm{nm}$ up to $169\,\mathrm{K}$ for $\lambda_{\mathrm{exc}} = 850\,\mathrm{nm}$. The former theoretically takes place under pumping at $1030\,\mathrm{nm}$ while the latter takes place under pumping at $1037\,\mathrm{nm}$. Probably, the contours obtained for $\lambda_{\mathrm{exc}} = 1028\,\mathrm{nm}$ are most applicable for laser cooling since $1028\,\mathrm{nm}$ is larger than λ_f, above which cooling is possible [64]. It is underlined that the Figure 33 does not say that anti-Stokes fluorescence cooling is possible when $\lambda_p < \lambda_f$.

Although using $\lambda_{\mathrm{exc}} > \lambda_f$ would be most representative of cooling performance,
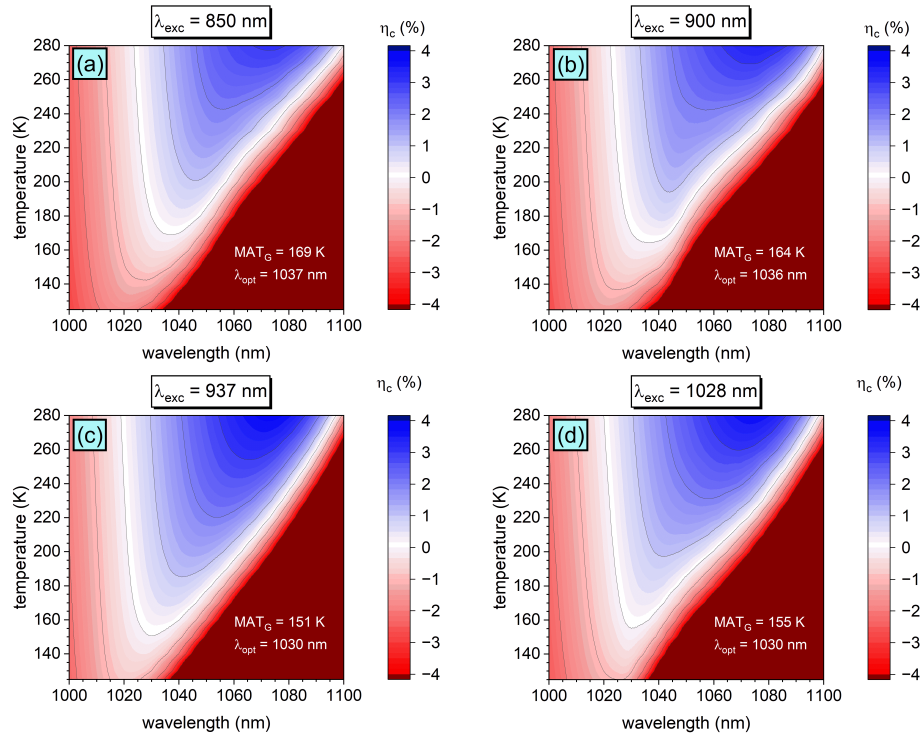
Figure 33: Cooling efficiency versus temperature and wavelength as obtained from evaluation of Equation 20 with parameters acquired from measurements made with different excitation wavelengths (a) 850 nm (b) 900 nm (c) 937 nm and (d) 1028 nm.

it would be more convenient and experimentally simpler to be able to obtain the cooling efficiency contour under short wavelength excitation. At $\lambda_{\text{exc}} > \lambda_f$, the absorption is low, and decreases significantly as the sample temperature drops. Low absorption makes the signal to noise ratio of spectroscopic measurements low as well as increases the prevalence of scattered unabsorbed excitation light in the measured spectra. Moreover, to remove the presence of scattered pump light, the spectra must be carefully interpolated which results in only approximate values. This is easy to do in the short wavelength region where, as can be seen well in Figure 30, a small sub-nm segment within the range 880-950 nm could easily be approximated with reasonable accuracy by a simple linear fit. However, as highlighted by Figure 28 and Figure 30, the long wavelength regime is highly sensitive and nonlinearly shaped, making interpolation an undesirable course of action. Despite what may be desirable, the results herein suggest that MAT contour plots should be carefully obtained at $\lambda_{\text{exc}} > \lambda_f$ when site-selective excitation behavior is present.

Taking advantage of the above mentioned benefits when employing $\lambda_{\text{exc}} < \lambda_f$ should still be valid when the material under consideration is insensitive to λ_{exc}. To confirm this, two additional material hosts were measured at different λ_{exc}. One was crystalline YLF doped with 1%Yb (black); the workhorse material of current optical refrigeration technology [22, 14, 74]. Second was a high performance ytterbium doped fluoride-phosphate glass ($6 \cdot 10^{26}$ Yb^{3+} ions per m^3, Yb:FP15, red) prepared by melt quenching developed for the POLARIS project (**P**etawatt **O**ptical **L**aser **A**mplifier for **R**adiation **I**ntensive Experiment**S**) [95, 96, 97, 98]. In Figure 34, the ytterbium emission linehsape is compared for different hosts under two different excitation wavelengths, 935 nm (solid) and 900 nm (dashed), at room temperature. The emission lineshapes from the investigated YLF and FP15 show no dependence on λ_{exc}. For the silica sample (Al:SiO$_2$, blue), the dependence on λ_{exc} is clear. Figure 34 indicates the standard methodology for determining the MAT of a material [99, 100, 69, 44],
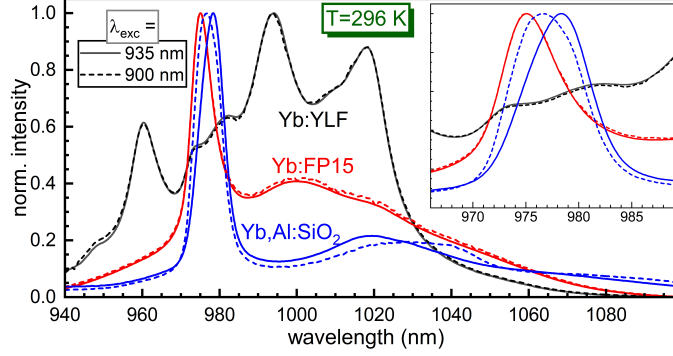
Figure 34: Emission spectra of ytterbium taken for λ_{exc}=935 nm (solid) and λ_{exc}=900 nm (dashed) in crystalline yttrium lithium fluoride (YLF, black), vitreous fluoride-phoshpate (FP15, red), and vitreous silica co-doped with aluminium (Al:SiO$_2$, blue).
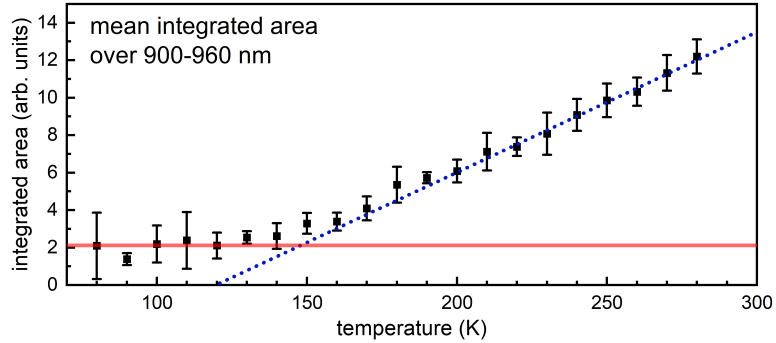
Figure 35: Mean integrated area between 900-960 nm at each temperature for all λ_{exc} in Figure 30. The lines are drawn to guide the eyes. The solid red line is a linear fit between 80 K and 130 K. The dotted blue line is a linear fit of the data above 200 K.

as pioneered by Sheik-Bahae and co-workers, remains applicable in cases previously studied.

A question that arises from this work is whether or not a general approach can be taken to evaluating the cooling potential of a host material. We do not attempt here to answer this question in entirety, but would like to present an analysis route that may have potential. Transitions from E$_6$ → E$_{1,2}$ have central wavelengths between 900-960 nm. E$_6$ is the thermally populated sub-level of the $^2F_{5/2}$ manifold. The laser cooling cycle requires long wavelength pumping from E$_{2,3,4}$ → E$_5$. This is followed by excited ytterbium ions absorbing host energy in the form of phonons, thus populating E$_6$. The radiative transition out of E$_6$ to the $^2F_{7/2}$ manifold is one path of

the laser cooling cycle that permits the fluorescence to cool the material, the other being $E_5 \rightarrow E_1$ transitions following long wavelength pumping. As the population of E_6 goes to zero with decreasing temperature, either due to lower internal temperature from optical refrigeration or lower external temperature due to the surrounding environment, so too will the cooling potential of the material. To represent this, the mean integrated area between 900-960 nm for all λ_{exc} (refer to Figure 30) is shown in Figure 35. The error bars represent the standard deviation of the individual λ_{exc} measurements. The fitted lines are intended to guide the eyes. The red line represents a linear fit of the data points between 80-130 K, where graphical inspection suggests the data is oscillating around a noise floor. The dotted blue line represents a linear fit of the data points above 200 K, where the temperature dependence is highly linear. The solid red and dotted blue lines intercept at 148 K. Such an intercept-method approach may empirically represent a semi-quantitative determination of the MAT for a host material under ideal conditions, though more samples of varying compositions need to be considered. A combination of this approach and the original MAT contour plot technique may be a robust approach to evaluating host materials for optical refrigeration when site-selective behavior is exhibited.

5.4   Conclusions

As laser cooling of silica glass gains increasing attention, the ability to compare results of different research groups is becoming increasingly important. In this context, site-selective excitation plays a non-trivial role. To elucidate the impact of site-selectivity in characterizing ytterbium doped silica, we carried out temperature-dependent site-selective spectroscopy using a cooling-grade Yb,Al co-doped silica rod. At 80 K, longer wavelength excitation probed sites with a weaker Stark splitting, as evidence by the contraction of the emission spectrum. The strongest emission band in the low temperature measurements could be described by two component bands at all

excitation wavelengths, which may be due to the ytterbium ions existing in two preferred site environments. The structural landscape of aluminosilicate glasses is quite rich [101, 102, 103], and it will require a coordinated effort to investigate this further and to clarify the impact it has, if any, on the cooling performance. Near room temperature, the mean fluorescence wavelength, λ_f, varied over roughly $4\,\text{nm}$ and the peak wavelength, λ_{peak}, by about $3\,\text{nm}$, depending on the excitation wavelength, λ_{exc}. Quantities calculated from the temperature-dependent emission spectra did not yield converging values when modeling the sample's cooling efficiency. When calculating the temperature-dependent cooling efficiency using the standard procedures [44, 69], the global minimum achievable temperature, MAT_G, of the investigated sample varies between 151-169 K for optimal pump wavelengths, λ_{opt}, between 1030-1037 nm. The results of this study show that in the context of materials exhibiting site-selective excitation, new techniques need to be developed for the precise characterization and modeling of rare-earth doped materials for solid-state optical refrigeration. However, many readers will also observe that the implications of the findings reported here extend beyond applications revolving around laser cooling silica. In particular, awareness of the dependence of the calculated absorption and emission cross-section on the excitation wavelength used for acquisition is of universal importance to fiber laser practitioners.

6   Power cooling to 229 K

6.1   Background

Chapter 2 contained cooling results of Sample B (Table 1) with up to 185 W of pump power, though with only marginal returns about ≈100 W. Chapter 3 identified Sample A, the more highly doped composition, as the better performing material for optical cooling. In Chapter 4, power cooling of Sample A by 41 K was carried out with 50 W of pump power, though Chapter 2 suggests more cooling could be achieved with greater pump power. The activity of Chapter 4 was limited by the available pump power. The amplifier used therein was constructed in 10/125 fiber architecture. Once above the 25-30 W output level, two main problems were often present - stimulated Brillouin scattering (SBS) and, to a lesser extent, overheating and subsequent breakdown of splices between passive fiber and gain fiber. The most prevalent issues, was mitigated to some extent in the previous work by using a two-tone seed, a slight temperature gradient across the gain fiber, a short gain fiber, and introducing a polarization controller into the passive delivery fiber segment following the gain fiber. Although these measures allowed maximum output up to 60 w at 1030 nm, and operation stable enough for experiments at 50 W output levels, it is obvious from Chapter 2 that to fully explore the cooling potential of these materials that about 100 W of power is required. This chapter describes the design of a high power amplifier that was constructed which output 97 W limited only by the available pump power.

6.2   Experimental

A detailed schematic of the fiber amplifier constructed is shown in Figure 36. The system begins with a single mode 500 mW 976 nm butterfly diode mounted in a compact
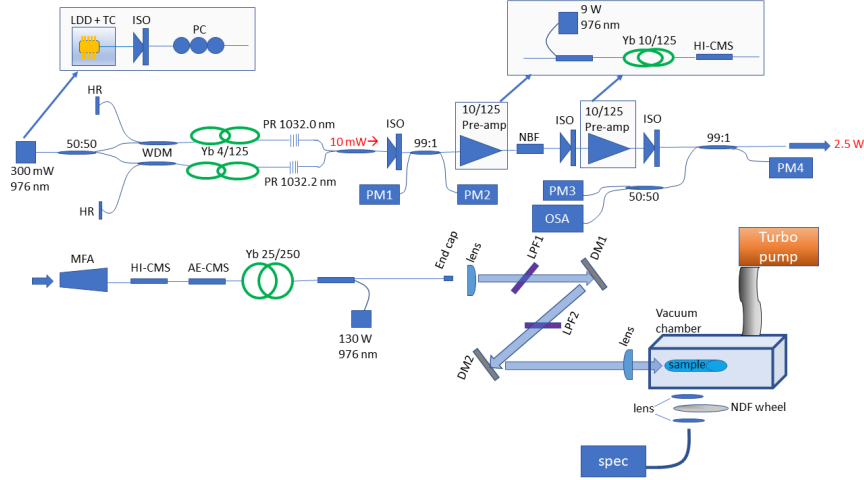
Figure 36: Schematic of 100 W 1032 nm amplifier. See text for details.

laser diode driver and temperature controller module (actual maximum output power close to 350 mW). The pigtailed diode is spliced to a 2 W 980 nm inline fiber isolator. The transmission of fiber couplers and wavelength division mulitplexers (WDMs) can be sensitive to the polarization of the input light, even in non-polarization maintaining fiber components, and so the forward pump fiber was inserted into a 2-inch diameter 3-paddle polarization controller.

The single mode pump light was split with a 3 dB coupler to simultaneously pump two fiber Bragg grating (FBG) laser cavities to create the two-tone seed. A single cavity had the following structure: The 976 nm pump was inserted into the 980 nm channel of a 980/1060 nm WDM. The common port leg of the WDM was spliced to about 50 cm of single mode 4/125 ytterbium doped gain fibers which was followed by a 50% reflectivity FBG. The bandwidth of both FBGs was 500 pm and the separation of their center wavelengths was 200 pm (1032.0 and 1032.2 nm). The FBG provided signal feedback and functioned as the output coupler. The oscillating signal propagating in the direction of the WDM traveled through the common port and exited the 1060 nm port where a broadband retroreflector served as a highly reflective mirror (R>96%). Note following the experiments in Chapter 4 where a similar seed was built using 1030.0 and 1030.2 nm FBGs, a need two-tone seed was built at 1032 nm. The

1030 nm was initially used as it was the center wavelength of multiple components used later down the line in the system but operation and experiments eventually led to the conclusion that a 1032 nm signal would ultimately work as well, which was a more optimal wavelength based off the results of Chapter 3. The two parallel laser cavities were combined with a 3 dB coupler.

The forward propagating signal was inserted into a 300 mW 1064 nm inline fiber isolator. A 20 dB 2x2 tap coupler was used to monitor the forward signal with power meter (PM2) and the back-reflection from the pre-amplifier stages (PM1). Two identical pre-amplifier stages were used. The pre-amplifiers consisted of a pump and signal combiner with 10/125 signal input/output and 105/125 pump legs. One pump leg was spliced to a 9 W wavelength stabilized 976 nm multimode pump diode. The pump and signal combiner was spliced to a 1.5 m length of 10/125 Yb doped gain fiber. Residual pump light in the cladding was removed by a high index epoxy coating on a roughly 2 cm length of fiber on either end of the splice to the following component. The first pre-amplifier was only operated at a pump level required to have about 1 W signal output achieved. This kept back-reflection toward the seed low. The amplified spontaneous emission (ASE) in the signal spectrum was cleaned up by the use of a narrowband pass filter (NBF) centered at 1030 nm with a 6 nm bandwidth. The cleaned up signal passes through a 10 W 1030 nm 10 nm bandwidth isolator. Insertion loss from the NBF and isolator reduce the forward power to about 600 mW. This signal is then re-amplified in a second pre-amp stage so that the power entering the main amplification stage is approximately 2.5 W.

Before the main amplifier stage, a 20 dB 2x2 coupler monitors the forward and backward propagating power. The backward tap is split once more with a 3 dB splitter to monitor on one channel the back reflected power and on the other channel the spectral content with an optical spectrum analyzer (OSA). The primary forward signal goes through a mode field adapter (MFA). The MFA takes the single mode

beam from a 10/125 fiber to a 25/250 fiber architecture. The larger core size was chosen because the SBS threshold power is direction proportional to the effective area [104]. 1.8 m of Nufern LMA-YDF-25/250 was used as the gain fiber in a reverse pumping configuration using a 130 W nLight 976 nm wavelength stabilized pump diode. The combiner to gain fiber splice was recoated manually with a low index epoxy (Coherent) in a copper V-groove in good contact with the aluminum breadboard underneath. The recoated splice was positioned below a blowing fan. The gain fiber to signal input splice was acid-etch (AE) using Armor Etch with 3 applications of 6 minute exposures and rinsing with deionized water in between. About 4 cm of fiber was etched in this way to function as a cladding mode stripper (CMS). This AE-CMS was suspended in air over a copper V-groove with a fan blowing on it. Because some low numerical aperture pump light may not be fully removed by the AE-CMS, some of the low index polymer coating was removed and a low-power splice protector was heat shrunk over the outer cladding of the fiber. The splice protector acts as a high-index CMS and to promote the leakage of low NA pump light. The splice protector was bent to have about a 5 cm radius of curvature to encourage the light to escape. Lastly, a short segment of coreless $250 \, \mu$m diameter fiber was spliced to the output end of the amplifier and cleaved at an angle of 7 degrees.

The output of the amplifier was collimated and steered with dielectric mirrors while passing through two long pass filters before being injected into the sample in the vacuum chamber held at 10^{-6}. It is worth noting that in between previous cooling experiments and these experiments, the sample was not removed from the chamber and had been under high vacuum for over one month during that span of time, suggesting any possible off-gasing by the sample had already taken place. The vacuum obtained in these experiments was about 1 order better than previous experiments, after using a flowing He and mass spectrometer leak detection routine to identify poor seals in the vacuum chamber.

The fluorescence was used for temperature measurements, as before. Following Chapter 5, it is underlined here that the experiments and calibration were both carried out using 1032 nm excitation. The fluorescence was collimated and attenuated with a continuous neutral density filter (NDF) wheel. For a given experiment, the NDF was adjusted for each pump power level so that the fluorescence power reaching the spectrometer was maximized without saturating the detector. The fluorescence was coupled into the $600\,\mu$m core step-index multimode fiber feeding a CCD spectrometer. The spectra were acquired on a computer every 500 ms with a 100 ms integration time.

6.3   Results and discussion

The performance of the amplifier is displayed by two figures of merit in Figure 37. In (a), the optical to optical conversion with respect to the launched pump power is linear with a slope of 78%. In (b), the wall-plug efficiency is calculated using the manufacturer specifications for the current and voltage and the measured output power of the amplifier. The electrical to optical efficiency is is about 35%.

Cooling experiments were conducted as before. The maximum change in temperature for different pump powers is shown in Figure 38. The cooling increases with increasing pump power, though at higher pump powers the magnitude of cooling per additional watt of pump starts to diminish.

The best result in Figure 38 is cooling by 67 K with 97 W of pump power. Spectral measurements acquired over the full recording spectrometer range are shown in Figure 39. For reference, the background is plotted in black. The red lineshape, being the first recorded spectrum, is taken as the room temperature spectrum. A small amount of cooperative upconversion luminescence is seen at around 518 nm, which is slightly decreased in the blue spectrum which was acquired at the end of the experiment.

The near-infrared fluorescence of the blue line is significantly reduced due to the
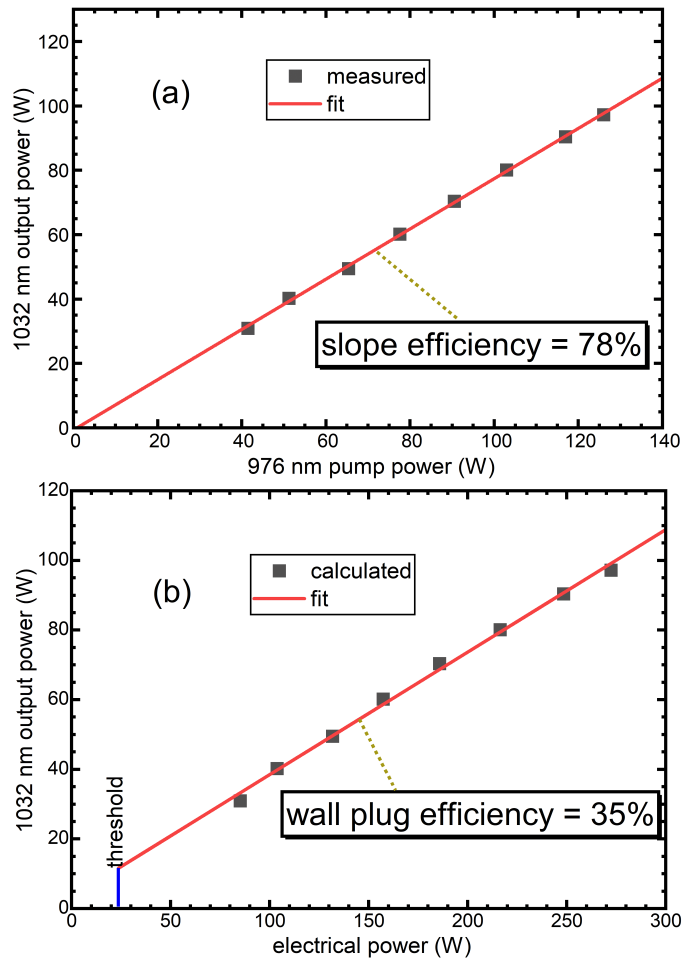
Figure 37: Efficiency plots of homemade amplifier: (a) optical to optical efficiency with respect to launched pump power and (b) electrical to optical efficiency.
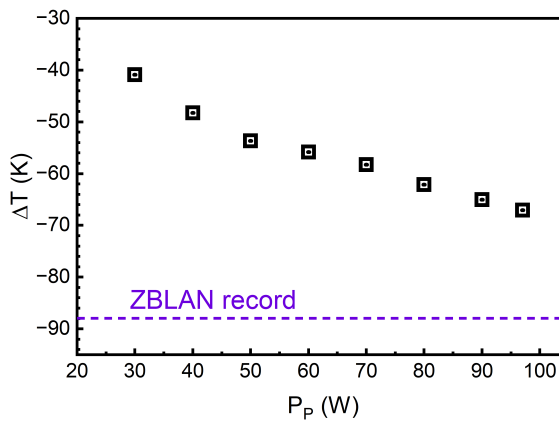
Figure 38: Change in temperature versus 1032 nm pump power. Horizontal dashed line represents ZBLAN record.
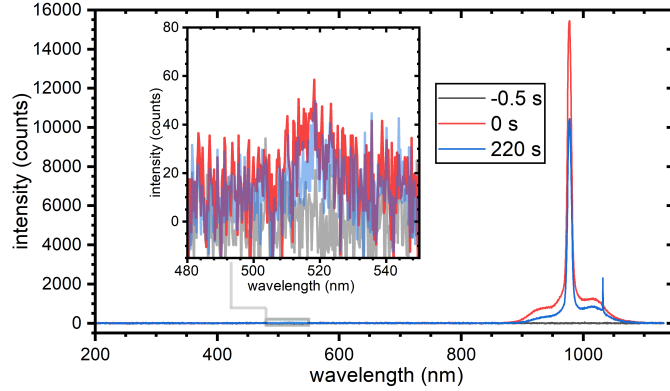
Figure 39: Measured spectrum over full instrument range immediately before pump was turned on (black), immediately after pump was turned on (red), and at the end of the experiment (blue).
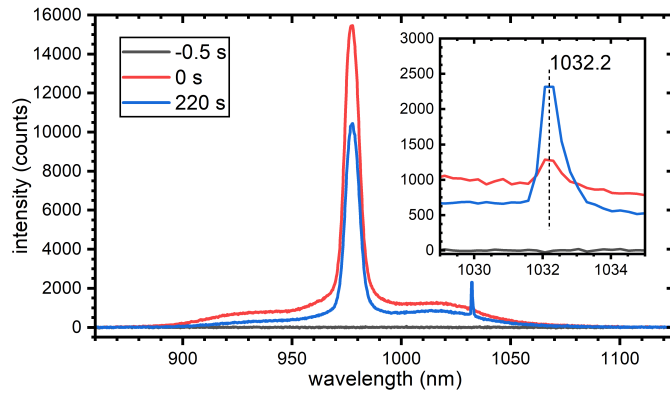
Figure 40: Measured spectrum in the Yb emission spectral range immediately before pump was turned on (black), immediately after pump was turned on (red), and at the end of the experiment (blue).

decrease in the resonant absorption with decreasing temperature which naturally results in a low fluorescence power. The near-infrared emission region is emphasized in Figure 40. As the absorption decreases, the scattered pump light reaching the spectrometer increases. This is highlighted by the inset where it can be seen that linewidth of the pump did not undergo significant broadening and still has a linewidth well below 1 nm.

Finally, the temporal cooling curve for the new record of ASF cooling in ytterbium doped silica is shown in Figure 41. The black circles represent experimentally measured data points. The red line represents an exponential fit of the data via
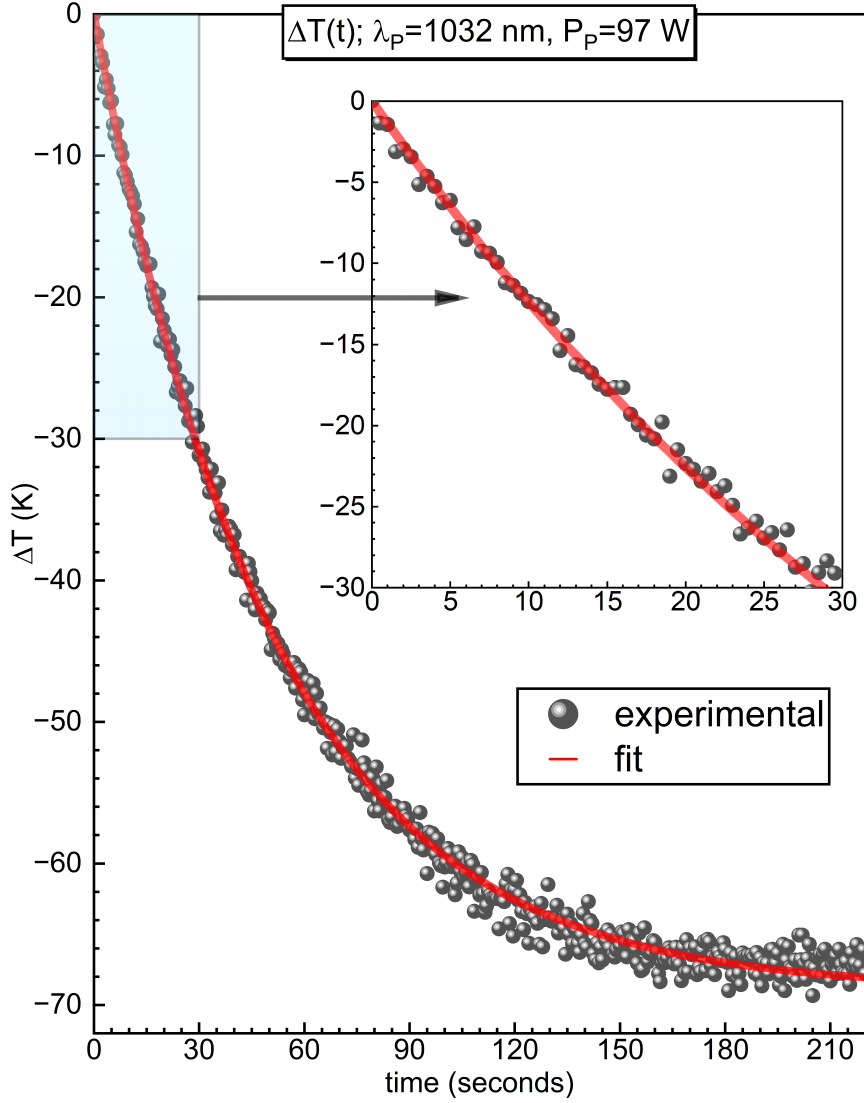
Figure 41: Experimentally measured cooling curve of Sample A subjected to the highest available pump power fit with single exponential.

$\Delta T(t) = \Delta T_{max} \left[\exp(-t/\tau) - 1\right]$. In this instance, ΔT_{max} and τ are fitting parameters and found to be $69\,\mathrm{K}$ and $50\,\mathrm{s}$, respectively. With these results, the future looks pretty cool for ytterbium doped silica.

7 Concluding remarks

7.1 Summary of work

Ytterbium doped silica fibers are the basis of many fiber laser systems used in industrial, medical, and defense settings. The high melting point of silica combined with the simple electronic structure of Yb^{3+} permits extremely efficient operation as well as the highest output power available in a fiber laser architecture. This doctoral dissertation entitled "High-power laser cooling and temperature-dependent fluorescence studies of ytterbium doped silica" has dealt with optical refrigeration experiments and associated characterization of Yb, Al co-doped silica rods. The main goal was to dethrone ZBLAN as the best performing glass for optical refrigeration, which although not achieved herein, seems to be well within reach now.

At the start of this project, laser cooling of silica glass was young, only being experimentally realized for the first time within the past two years. The lowest temperature achieved was cooling by 6 K from room temperature (RT) in high vacuum, compared to the 88 K from RT seen in ZBLAN in 2005. Laser cooling of silica in particular has promise for ultra-stable laser cavities, prevision metrology, and most obviously as a method of heat mitigation in integrated photonics and higher power laser systems.

Initial laser cooling experiments were carried out with sample A having dopant density $6.56 \cdot 10^{25}$ Yb^{3+} per m^3 (sample A) and Al:Yb ratio of 6:1 placed in a chamber held at high vacuum and supported on a fiber support system, to minimize the convective and conductive heat loads, respectively. Temperature measurements were made with a non-contact method of either thermal camera imaging or Differential Luminescence Thermometry (DLT). The maximum available power at the time was 20 W at 1035 nm. At atmospheric pressure, cooling by 3.6 K from RT was recorded

using a thermal camera. Cooling by 18 K from RT was measured in vacuum using DLT. Through analysis of the cooling onset in data obtained at different pump powers, the cooling efficiency, $\eta_c(\lambda = 1035\,\mathrm{nm})$, of the sample was determined by comparing the change in temperature to the absorbed power and was found to be 1.2% at λ_p=1035 nm.

LITMoS tests on both compositions measured cross-over wavelengths between 1018-1021 nm giving η_{ext} of both samples to be $\approx$0.99. By normalizing the change in temperature to the input pump power at each wavelength, it was shown that the optimal pumping wavelength occurred between $1032-1035\,\mathrm{nm}$. The more highly doped sample showed better pump power normalized cooling performance and so became the sole subject of the following high-power experiments.

A multi-stage amplifier was constructed in the Master Oscillator - Power Amplifier (MOPA) configuration using a homemade two-tone fiber laser as a seed source. Typical issues were encountered in the amplifier construction that needed to be overcome – thermal issues causing splices to break and SBS limiting output. After trial and error for many months, eventually 50 W output at 1030 nm was achieved and stable enough to carry out experiments. Sample A was cooled by 41 K from RT in high vacuum (10^{-5} torr) with 50 W of pump power. A new seed oscillator at 1032 nm and a new power amplifier utilizing a larger fiber core were later constructed. The best power cooling results obtained in this work showed cooling by 67 K from room temperature, a 10-fold improvement over the record at the start of this undertaking.

Temperature-dependent spectroscopic measurements of the emission lineshape and fluorescence lifetimes allowed computation of $\eta_c(\lambda, T)$, employing the previously measured η_{ext}. The global MAT was found to be around 150 K. An observation was made during the low temperature spectroscopy studies that raised questions about the local environment of the Yb ions. Under 940 nm excitation, the zero-phonon line transition was highly asymmetric at low temperatures. The feature was well-described

by fitting with two component bands spaced approximately $40\,\mathrm{cm}^{-1}$ apart. This spacing is comparable to the same transition for Yb^{3+} doped crystalline rare-earth orthosilicates and alkaline earth scandates, where the Yb^{3+} ions occupy two distinct crystallographic sites, and the fluorescence spectra is subsequently constructed from the superposition of both Stark manifolds. This led to further exploration of the spectroscopic behavior which revealed that the samples also exhibited site-selective excitation and that the emission spectral lineshapes, and therefore also $\lambda_f(T)$, were extremely sensitive to the excitation wavelength. The emission spectra versus temperature were measured again at multiple wavelengths and non-unique MATs were subsequently calculated. This has necessitated a re-evaluation of the application of the MAT procedure that has, until now, been used successfully for characterizing materials for solid-state optical refrigeration.

7.2   Future directions

Future power cooling experiments may be improve upon these results. A water cooled clam shell coated in a material highly absorptive around $1\,\mu$m and with low emissivity near $10\,\mu$m would lower the radiative lead. A more highly doped composition should allow greater cooling, but this may come along with a decrease in the external quantum efficiency. The two compositions investigated are quite similar and do not allow definitive conclusions to be drawn for composition optimization. Experiments varying beam shape may permit a higher fill factor of the pump in the sample, thereby both reducing overall local intensity and maximizing the number of Yb ions participating in the cooling process. A more costly route may employ deposition of spectrally selective dielectric coatings on the facets of an existing sample to confine pump light and achieve a multi-pass geometry without worrying about feedback into the fiber amplifier. A double-pass geometry with an external mirror would be possible if a free-space isolator is inserted in the setup after the amplifier output, though more

pump power would need to be available to offset the insertion loss of the isolator.

Fundamental questions also remain. Does the background absorption of cooling grade Yb doped silica decrease with temperature? Are two main local environments of the Yb ions the reasons for the two component bands of the zero-phonon line transition? Is this related to the presence of the Al cations and, if so, how? If there are two environments, can this be leveraged for enhanced cooling such as with two judiciously selected pump wavelengths? Or, does the spectral broadening resulting from more than one unique site environment pose undesirable limitations on the maximum cooling ability? Regarding the attainment of a figure of merit for a composition or sample, in light of site-selective fluorescence behavior, is there a methodology that can lead to converging solutions?

References

[1] K.S. Ramanm C.V., Krishnan. A new type of secondary radiation. <u>Nature</u>, 121(3048):501–502, 1928.

[2] Peter Pringsheim. Zwei bemerkungen über den unterschied von lumineszenz- und temperaturstrahlung. <u>Zeitschrift für Physik</u>, 57(11-12):739–746, 1929.

[3] T Kushida and JE Geusic. Optical refrigeration in Nd-doped yttrium aluminum garnet. <u>Physical Review Letters</u>, 21(16):1172, 1968.

[4] MA Weinstein. Thermodynamic limitation on the conversion of heat into light. <u>JOSA</u>, 50(6):597–602, 1960.

[5] Bauke Heeg, Peter A DeBarber, and Garry Rumbles. Influence of fluorescence reabsorption and trapping on solid-state optical cooling. <u>Applied optics</u>, 44(15):3117–3124, 2005.

[6] XL Ruan and M Kaviany. Enhanced laser cooling of rare-earth-ion-doped nanocrystalline powders. <u>Physical Review B</u>, 73(15):155422, 2006.

[7] S. R. Bowman, S. P. O'Connor, S. Biswal, N. J. Condon, and A. Rosenberg. Minimizing heat generation in solid-state lasers. <u>IEEE J. Quantum Electron</u>, 46:1076–1085, 2010.

[8] Esmaeil Mobini. <u>Radiation-Balanced Fiber Lasers and Amplifiers</u>. PhD thesis, The University of New Mexico, 2020.

[9] Esmaeil Mobini, Saeid Rostami, Mostafa Peysokhan, Alexander Albrecht, Stefan Kuhn, Sigrun Hein, Christian Hupel, Johannes Nold, Nicoletta Haarlammert, Thomas Schreiber, et al. Laser cooling of ytterbium-doped silica glass. <u>Communications Physics</u>, 3(1):1–6, 2020.

[10] Michel Poulain, Marcel Poulain, and Jacques Lucas. Verres fluores au tetrafluorure de zirconium proprietes optiques d'un verre dope au Nd^{3+}. Materials Research Bulletin, 10(4):243–246, 1975.

[11] Alexis G. Clare, Peter F. Wachtel, and J. David Musgraves. Halide Glasses, pages 595–616. Springer International Publishing, Cham, 2019.

[12] Richard I Epstein, Melvin I Buchwald, Bradley C Edwards, Timothy R Gosnell, and Carl E Mungan. Observation of laser-induced fluorescent cooling of a solid. Nature, 377(6549):500–503, 1995.

[13] Rémi Vicente. Optical cryocooler design and demonstration for space applications. PhD thesis, Université Grenoble Alpes, 2021.

[14] Rémi Vicente, Giovanni Cittadino, Alberto Di Lieto, Mauro Tonelli, Arnaud Gardelein, and Gilles Nogues. Operation of a fiber-coupled laser cooled down to cryogenic temperatures. Optics Express, 30(8):12929–12936, 2022.

[15] CE Mungan, MI Buchwald, BC Edwards, RI Epstein, and TR Gosnell. Laser cooling of a solid by 16 K starting from room temperature. Physical review letters, 78(6):1030, 1997.

[16] X Luo, MD Eisaman, and TR Gosnell. Laser cooling of a solid by 21 K starting from room temperature. Optics Letters, 23(8):639–641, 1998.

[17] TR Gosnell. Laser cooling of a solid by 65 K starting from room temperature. Optics Letters, 24(15):1041–1043, 1999.

[18] J Thiede, J Distel, SR Greenfield, and RI Epstein. Cooling to 208 K by optical refrigeration. Applied Physics Letters, 86(15):154107, 2005.

[19] Denis V Seletskiy, Seth D Melgaard, Richard I Epstein, Alberto Di Lieto, Mauro Tonelli, and Mansoor Sheik-Bahae. Local laser cooling of Yb : YLF to 110 K. Optics express, 19(19):18229–18236, 2011.

[20] Seth D Melgaard, Alexander R Albrecht, Markus P Hehlen, and Mansoor Sheik-Bahae. Solid-state optical refrigeration to sub-100 kelvin regime. Scientific reports, 6(1):1–6, 2016.

[21] Stefan Püschel, Felix Mauerhoff, Christian Kränkel, and Hiroki Tanaka. Solid-state laser cooling in Yb : CaF$_2$ and Yb : SrF$_2$ by anti-Stokes fluorescence. Optics Letters, 47(2):333–336, 2022.

[22] Markus P Hehlen, Junwei Meng, Alexander R Albrecht, Eric R Lee, Aram Gragossian, Steven P Love, Christopher E Hamilton, Richard I Epstein, and Mansoor Sheik-Bahae. First demonstration of an all-solid-state optical cryocooler. Light: Science & Applications, 7(1):15, 2018.

[23] Zhou Yang, Junwei Meng, Alexander R Albrecht, and Mansoor Sheik-Bahae. Radiation-balanced yb: Yag disk laser. Optics express, 27(2):1392–1400, 2019.

[24] Jackson L Kock, Alexander R Albrecht, Richard I Epstein, and Mansoor Sheik-Bahae. Optical refrigeration of payloads to t< 125 k. Optics Letters, 47(18):4720–4723, 2022.

[25] Jackson Kock, Alexander Albrecht, Duncan McGraw, Richard Epstein, and Mansoor Sheik-Bahae. Payload cooling to< 125k using optical refrigeration in yb: Ylf. In Photonic Heat Engines: Science and Applications V, page PC1243706. SPIE, 2023.

[26] Jennifer M Knall, Magnus Engholm, Tommy Boilard, Martin Bernier, and Michel JF Digonnet. Radiation-balanced silica fiber amplifier. Physical Review Letters, 127(1):013903, 2021.

[27] J Knall, Magnus Engholm, T Boilard, M Bernier, P-B Vigneron, N Yu, PD Dragic, J Ballato, and MJF Digonnet. Radiation-balanced silica fiber laser. Optica, 8(6):830–833, 2021.

[28] S.R. Bowman. Lasers without internal heat generation. IEEE Journal of Quantum Electronics, 35(1):115–122, 1999.

[29] Nader A Naderi, Iyad Dajani, and Angel Flores. High-efficiency, kilowatt 1034 nm all-fiber amplifier operating at 11 pm linewidth. Optics Letters, 41(5):1018–1021, 2016.

[30] F. Beier, C. Hupel, S. Kuhn, S. Hein, J. Nold, F. Proske, B. Sattler, A. Liem, C. Jauregui, J. Limpert, N. Haarlammert, T. Schreiber, R. Eberhardt, and A. Tünnermann. Single mode 4.3 kw output power from a diode-pumped yb-doped fiber amplifier. Opt. Express, 25:14892–14899, 2017.

[31] F. Beier, F. Möller, B. Sattler, J. Nold, A. Liem, C. Hupel, S. Kuhn, S. Hein, N. Haarlammert, T. Schreiber, R. Eberhardt, , and A. Tünnermann. Experimental investigations on the tmi thresholds of low-na yb-doped single-mode fibers. Opt. Lett., 43:1291–1294, 2018.

[32] Cesar Jauregui, Christoph Stihler, and Jens Limpert. Transverse mode instability. Advances in Optics and Photonics, 12(2):429–484, 2020.

[33] Denis V Seletskiy, Richard Epstein, and Mansoor Sheik-Bahae. Laser cooling in solids: advances and prospects. Reports on Progress in Physics, 79(9):096401, 2016.

[34] Mostafa Peysokhan, Esmaeil Mobini, Arman Allahverdi, Behnam Abaie, and Arash Mafi. Characterization of yb-doped zblan fiber as a platform for radiation-balanced lasers. Photonics Research, 8(2):202–210, 2020.

[35] Michael Thomas Murtagh. Compositional investigation of Yb^{3+}-doped glasses for laser-induced fluorescent cooling applications. Rutgers The State University of New Jersey-New Brunswick, 1999.

[36] A Winterstein-Beckmann, D Möncke, D Palles, EI Kamitsos, and L Wondraczek. Raman spectroscopic study of structural changes induced by micro-indentation in low alkali borosilicate glasses. Journal of non-crystalline solids, 401:110–114, 2014.

[37] D Möncke and D Ehrt. Structure and properties of mixed phosphate and fluoride glasses. Physics and chemistry of glasses, 46(2):67–71, 2005.

[38] I Efthimiopoulos, D Palles, S Richter, U Hoppe, Doris Möncke, L Wondraczek, S Nolte, and EI Kamitsos. Femtosecond laser-induced transformations in ultra-low expansion glass: Microstructure and local density variations by vibrational spectroscopy. Journal of Applied Physics, 123(23):233105, 2018.

[39] Esmaeil Mobini, Mostafa Peysokhan, Behnam Abaie, Markus P Hehlen, and Arash Mafi. Spectroscopic investigation of yb-doped silica glass for solid-state optical refrigeration. Physical Review Applied, 11(1):014066, 2019.

[40] Esmaeil Mobini, Saeid Rostami, Mostafa Peysokhan, Alexander Albrecht, Stefan Kuhn, Sigrun Hein, Christian Hupel, Johannes Nold, Nicoletta Haarlammert, Thomas Schreiber, et al. Laser cooling of silica glass. arXiv preprint arXiv:1910.10609, 2019.

[41] Jennifer Knall, Pierre-Baptiste Vigneron, Magnus Engholm, Peter D. Dragic, Nanjie Yu, John Ballato, Martin Bernier, and Michel J. F. Digonnet. Laser cooling in a silica optical fiber at atmospheric pressure. Opt. Lett., 45(5):1092–1095, Mar 2020.

[42] Mostafa Peysokhan, Saeid Rostami, Esmaeil Mobini, Alexander R Albrecht, Stefan Kuhn, Sigrun Hein, Christian Hupel, Johannes Nold, Nicoletta Haarlammert, Thomas Schreiber, et al. Implementation of laser-induced anti-stokes fluorescence power cooling of ytterbium-doped silica glass. ACS omega, 6(12):8376–8381, 2021.

[43] Jennifer Knall, Magnus Engholm, John Ballato, Peter D. Dragic, Nanjie Yu, and Michel J. F. Digonnet. Experimental comparison of silica fibers for laser cooling. Opt. Lett., 45(14):4020–4023, Jul 2020.

[44] Azzurra Volpi, Junwei Meng, Aram Gragossian, Alexander R Albrecht, Saeid Rostami, Alberto Di Lieto, Richard I Epstein, Mauro Tonelli, Markus P Hehlen, and Mansoor Sheik-Bahae. Optical refrigeration: the role of parasitic absorption at cryogenic temperatures. Optics Express, 27(21):29710–29718, 2019.

[45] John Ballato and Peter D Dragic. The uniqueness of glass for passive thermal management for optical fibers. International Journal of Applied Glass Science, 13(3):267–280, 2022.

[46] Jennifer M Knall, Mina Esmaeelpour, and Michel JF Digonnet. Model of anti-stokes fluorescence cooling in a single-mode optical fiber. Journal of Lightwave Technology, 36(20):4752–4760, 2018.

[47] Benjamin N Frey, Enkeleda Balliu, Pierre-Baptiste Vigneron, Jenny Knall, Thomas W Hawkins, Bailey Meehan, Mary Ann Cahoon, John Ballato, Magnus Engholm, Peter D Dragic, et al. Cooling yb-doped silica fibers and fiber lasers using anti-stokes pumping. In Photonic Heat Engines: Science and Applications V, volume 12437, pages 29–36. SPIE, 2023.

[48] J Ballato, TW Hawkins, PD Dragic, M Engholm, MJF Digonnet, and L Dong. Material approaches to thermal management in advanced fiber lasers and am-

plifiers. In Photonic Heat Engines: Science and Applications V, volume 12437, pages 16–22. SPIE, 2023.

[49] Jyothis Thomas, Thomas Meyneng, Amirhossein Tehranchi, Nicolas Gregoire, Frederic Monet, Denis Seletskiy, Younès Messaddeq, and Raman Kashyap. Demonstration of laser cooling in a novel all oxide gayy silica glass. Scientific Reports, 13(1):5436, 2023.

[50] Pierre-Baptiste Vigneron, Bailey Meehan, Mary Ann Cahoon, Thomas W Hawkins, John Ballato, Peter D Dragic, Magnus Engholm, Tommy Boilard, Martin Bernier, and Michel JF Digonnet. Anti-stokes fluorescence cooling of nanoparticle-doped silica fibers. Optics Letters, 47(10):2590–2593, 2022.

[51] Xiaojing Xia, Anupum Pant, E James Davis, and Peter J Pauzauskie. Design of a radiation-balanced fiber laser via optically active composite cladding materials. JOSA B, 36(12):3307–3314, 2019.

[52] Esmaeil Mobini, Mostafa Peysokhan, and Arash Mafi. Heat mitigation of a core/cladding yb-doped fiber amplifier using anti-stokes fluorescence cooling. JOSA B, 36(8):2167–2177, 2019.

[53] Jennifer M Knall and Michel JF Digonnet. Design of high-power radiation-balanced silica fiber lasers with a doped core and cladding. Journal of Lightwave Technology, 39(8):2497–2504, 2021.

[54] Mostafa Peysokhan, Esmaeil Mobini, and Arash Mafi. Analytical formulation of a high-power yb-doped double-cladding fiber laser. OSA Continuum, 3(7):1940–1951, 2020.

[55] S Kuhn, S Hein, C Hupel, J Nold, F Stutzki, N Haarlammert, T Schreiber, R Eberhardt, and A Tünnermann. High-power fiber laser materials: influ-

ence of fabrication methods and codopants on optical properties. In <u>Optical Components and Materials XVI</u>, volume 10914, pages 27–39. SPIE, 2019.

[56] Kazuo Arai, Hiroshi Namikawa, Ken Kumata, Tatsutoku Honda, Yoshiro Ishii, and Takashi Handa. Aluminum or phosphorus co-doping effects on the fluorescence and structural properties of neodymium-doped silica glass. <u>Journal of Applied Physics</u>, 59(10):3430–3436, 1986.

[57] Andreas Herrmann, Stefan Kuhn, Mirko Tiegel, Christian Rüssel, Jörg Körner, Diethard Klöpfel, Joachim Hein, and Malte C Kaluza. Structure and fluorescence properties of ternary aluminosilicate glasses doped with samarium and europium. <u>Journal of Materials Chemistry C</u>, 2(21):4328–4337, 2014.

[58] Babak Imangholi, Michael P Hasselbeck, Daniel A Bender, Chengao Wang, Mansoor Sheik-Bahae, Richard I Epstein, and Sarah Kurtz. Differential luminescence thermometry in semiconductor laser cooling. In <u>Physics and Simulation of Optoelectronic Devices XIV</u>, volume 6115, pages 215–220. SPIE, 2006.

[59] DE McCumber. Einstein relations connecting broadband emission and absorption spectra. <u>Physical Review</u>, 136(4A):A954, 1964.

[60] Nanjie Yu and Peter D Dragic. On the use of brillouin scattering to evaluate quantum conversion efficiency in yb-doped optical fibers. <u>Journal of Lightwave Technology</u>, 39(12):4158–4165, 2021.

[61] Pascal Paradis, Tommy Boilard, Vincent Fortin, Stanislaw Trzesien, Michèle Ude, Bernard Dussardier, Réal Vallée, and Martin Bernier. Dysprosium-doped silica fiber as saturable absorber for mid-infrared pulsed all-fiber lasers. <u>Optics Express</u>, 30(3):3367–3378, 2022.

[62] Gonzalo Palma-Vega, Till Walbaum, Matthias Heinzig, Stefan Kuhn, Christian Hupel, Sigrun Hein, Gerrit Feldkamp, Bettina Sattler, Johannes Nold, Nicoletta Haarlammert, et al. Ring-up-doped fiber for the generation of more than 600 w single-mode narrow-band output at 1018 nm. Optics Letters, 44(10):2502–2505, 2019.

[63] Brian Topper, Mostafa Peysokhan, Alexander R Albrecht, Angel S Flores, Stefan Kuhn, Denny Hässner, Sigrun Hein, Christian Hupel, Johannes Nold, Nicoletta Haarlammert, et al. Laser cooling of a yb doped silica fiber by 18 kelvin from room temperature. Optics Letters, 46(22):5707–5710, 2021.

[64] Brian Topper, Alexander Neumann, Alexander R Albrecht, Angel S Flores, Stefan Kuhn, Denny Häßner, Sigrun Hein, Christian Hupel, Johannes Nold, Nicoletta Haarlammert, et al. Laser cooling experiments to measure the quantum efficiency of yb-doped silica fibers. Optics Letters, 47(14):3608–3611, 2022.

[65] Galina Nemova and Raman Kashyap. Optimization of the dimensions of an Yb^{3+} : ZBLANP optical fiber sample for laser cooling of solids. Optics letters, 33(19):2218–2220, 2008.

[66] Johannes Kirchhof, Sonja Unger, and Bruno Knappe. Fluorine containing high-silica glasses for speciality optical fibers. Advanced Materials Research, 39-40:265 – 268, 2008.

[67] W Patterson, E Soto, M Fleharty, and M Sheik-Bahae. Differential luminescence thermometry in laser cooling of solids. In Laser Cooling of Solids, volume 6461, pages 50–55. SPIE, 2007.

[68] Denis V Seletskiy, Seth D Melgaard, Stefano Bigotta, Alberto Di Lieto, Mauro Tonelli, and Mansoor Sheik-Bahae. Laser cooling of solids to cryogenic temperatures. Nature Photonics, 4(3):161–164, 2010.

[69] Denis V Seletskiy, Seth D Melgaard, Richard I Epstein, Alberto Di Lieto, Mauro Tonelli, and Mansoor Sheik-Bahae. Precise determination of minimum achievable temperature for solid-state optical refrigeration. Journal of luminescence, 133:5–9, 2013.

[70] JC Walling, O Peterson, H Jenssen, RC Morris, and E O'Dell. Tunable alexandrite lasers. IEEE Journal of Quantum Electronics, 16(12):1302–1315, 1980.

[71] TC Newell, P Peterson, A Gavrielides, and MP Sharma. Temperature effects on the emission properties of yb-doped optical fibers. Optics communications, 273(1):256–259, 2007.

[72] T Schreiber, S Kuhn, G Feldkamp, A Schwuchow, K Schuster, S Hein, R Eberhardt, and A Tünnermann. Micro-fluorescence lifetime and spectral imaging of ytterbium doped laser materials. Optics express, 26(25):32417–32432, 2018.

[73] Anka Schwuchow, Sonja Unger, Sylvia Jetschke, and Johannes Kirchhof. Advanced attenuation and fluorescence measurement methods in the investigation of photodarkening and related properties of ytterbium-doped fibers. Appl. Opt., 53(7):1466–1473, Mar 2014.

[74] Stefan Püschel, Sascha Kalusniak, Christian Kränkel, and Hiroki Tanaka. Temperature-dependent radiative lifetime of yb: Ylf: refined cross sections and potential for laser cooling. Optics Express, 29(7):11106–11120, 2021.

[75] Xuelu Zou and Hisayoshi Toratani. Evaluation of spectroscopic properties of yb 3+-doped glasses. Physical review B, 52(22):15889, 1995.

[76] Gang Lei, J.E. Anderson, M.I. Buchwald, B.C. Edwards, R.I. Epstein, M.T. Murtagh, and G.H. Sigel. Spectroscopic evaluation of Yb^{3+}-doped glasses for optical refrigeration. IEEE Journal of Quantum Electronics, 34(10):1839–1845, 1998.

[77] Azzurra Volpi, Karl W. Krämer, Daniel Biner, Brenden Wiggins, Jackson Kock, Alexander R. Albrecht, Eric J. Peterson, Michael N. Spilde, Mansoor Sheik-Bahae, and Markus P. Hehlen. Bridgman growth of laser-cooling-grade $LiLuF_4$: Yb^{3+} single crystals. Crystal Growth & Design, 21(4):2142–2153, 2021.

[78] OK Alimov, TT Basiev, Yu K Voron'ko, Yu V Gribkov, A Ya Karasik, VV Osiko, AM Prokhorov, and IA Shcherbakov. Selective-laser-excitation study of the structure of inhomogeneously broadened spectra of nd 3+ ions in glass. Soviet Journal of Experimental and Theoretical Physics, 47:29–34, 1978.

[79] P Babu, Kyoung Hyuk Jang, Hyo Jin Seo, and CK Jayasankar. Optical and site-selective spectral studies of eu 3+-doped zinc oxyfluorotellurite glass. Journal of applied physics, 99(5):053522, 2006.

[80] MT Harrison and RG Denning. Site selective spectroscopy and molecular dynamics simulation of eu (iii) zblan glasses. Journal of luminescence, 69(5-6):265–285, 1996.

[81] Raffaella Rolli, Giorgio Samoggia, Marco Bettinelli, Adolfo Speghini, and Mario Wachtler. Site-selective spectroscopy of eu3+ doped lead germanate glasses. Journal of non-crystalline solids, 288(1-3):114–120, 2001.

[82] Sylvain Magne, Youcef Ouerdane, Michel Druetta, Jean-Pierre Goure, Pierre Ferdinand, and Gérard Monnom. Cooperative luminescence in an ytterbium-doped silica fibre. Optics communications, 111(3-4):310–316, 1994.

[83] OK Alimov, TT Basiev, VA Konushkin, AG Papashvili, A Ya Karasik, and L Henry. Investigations of yb-doped optical fiber using selective laser excitation. Applied Physics B, 104:845–850, 2011.

[84] Sacha Welinski, Alban Ferrier, Mikael Afzelius, and Philippe Goldner. High-resolution optical spectroscopy and magnetic properties of yb 3+ in y 2 sio 5. Physical Review B, 94(15):155116, 2016.

[85] S Campos, A Denoyer, S Jandl, B Viana, D Vivien, P Loiseau, and B Ferrand. Spectroscopic studies of yb3+-doped rare earth orthosilicate crystals. Journal of Physics: Condensed Matter, 16(25):4579, 2004.

[86] R Gaume, B Viana, J Derouet, and D Vivien. Spectroscopic properties of yb-doped scandium based compounds yb: Casc2o4, yb: Srsc2o4 and yb: Sc2sio5. Optical Materials, 22(2):107–115, 2003.

[87] Brian Topper, Alexander Neumann, Alexander R Albrecht, Angel S Flores, Stefan Kuhn, Denny Häßner, Sigrun Hein, Christian Hupel, Johannes Nold, Nicoletta Haarlammert, et al. Potential of ytterbium doped silica glass for solid-state optical refrigeration to below 200 k. Optics Express, 31(2):3122–3133, 2023.

[88] G Lei, JE Anderson, MI Buchwald, BC Edwards, and RI Epstein. Determination of spectral linewidths by voigt profiles in yb 3+-doped fluorozirconate glasses. Physical Review B, 57(13):7673, 1998.

[89] Andreas Herrmann, Günter Völksch, and Doris Ehrt. Tb3+ as probe ion—clustering and phase separation in borate and borosilicate glasses. International Journal of Applied Glass Science, 10(4):532–545, 2019.

[90] Katrin Thieme, Christian Patzig, Brian Topper, Christian Thieme, Stephan Gierth, Christian Rüssel, and Thomas Höche. Early-stage clustering in tb-doped borosilicate glasses revealed by high resolution scanning transmission electron microscopy and luminescence properties. Journal of Alloys and Compounds, page 171091, 2023.

[91] Mostafa Peysokhan, Esmaeil Mobini, Behnam Abaie, and Arash Mafi. Method for measuring the resonant absorption coefficient of rare-earth-doped optical fibers. Applied Optics, 58(7):1841–1846, 2019.

[92] Markus P Hehlen, Richard I Epstein, and Hiroyuki Inoue. Model of laser cooling in the yb 3+-doped fluorozirconate glass zblan. Physical Review B, 75(14):144302, 2007.

[93] Markus P Hehlen, Mansoor Sheik-Bahae, Richard I Epstein, Seth D Melgaard, and Denis V Seletskiy. Materials for optical cryocoolers. Journal of Materials Chemistry C, 1(45):7471–7478, 2013.

[94] Mansoor Sheik-Bahae and Richard I Epstein. Optical refrigeration. nature photonics, 1(12):693–699, 2007.

[95] Doris Ehrt and Thomas Toepfer. Preparation, structure, and properties of yb3+ fp laser glass. In Inorganic Optical Materials II, volume 4102, pages 95–105. SPIE, 2000.

[96] Doris Ehrt. Fluoroaluminate glasses for lasers and amplifiers. Current Opinion in Solid State and Materials Science, 7(2):135–141, 2003.

[97] Doris Ehrt. Phosphate and fluoride phosphate optical glasses—properties, structure and applications. Physics and Chemistry of Glasses-European Journal of Glass Science and Technology Part B, 56(6):217–234, 2015.

[98] Doris Möncke and Hellmut Eckert. Review on the structural analysis of fluoride-phosphate and fluoro-phosphate glasses. Journal of Non-Crystalline Solids: X, 3:100026, 2019.

[99] Saeid Rostami, Alexander R Albrecht, Azzurra Volpi, and Mansoor Sheik-Bahae. Observation of optical refrigeration in a holmium-doped crystal. Photonics Research, 7(4):445–451, 2019.

[100] Saeid Rostami, Alexander R Albrecht, Azzurra Volpi, Markus P Hehlen, Mauro Tonelli, and Mansoor Sheik-Bahae. Tm-doped crystals for mid-ir optical cryocoolers and radiation balanced lasers. Optics letters, 44(6):1419–1422, 2019.

[101] Stephen K Wilke, Chris J Benmore, Vrishank Menon, Jan Ilavsky, Aram Rezikyan, Randall E Youngman, Michael P Carson, and Richard Weber. Revisiting metastable immiscibility in sio2–al2o3: Structure and phase separation of supercooled liquids and glasses. Journal of the American Ceramic Society, 106(5):2820–2834, 2023.

[102] Amarnath R Allu, Anuraag Gaddam, Sudheer Ganisetti, Sathravada Balaji, Renée Siegel, Glenn C Mather, Margit Fabian, Maria J Pascual, Nicoletta Ditaranto, Wolfgang Milius, et al. Structure and crystallization of alkaline-earth aluminosilicate glasses: prevention of the alumina-avoidance principle. The Journal of Physical Chemistry B, 122(17):4737–4747, 2018.

[103] Baltzar Stevensson, Aleksander Jaworski, and Mattias Edén. The structural roles of sc and y in aluminosilicate glasses probed by molecular dynamics simulations. Journal of Non-Crystalline Solids, 460:36–46, 2017.

[104] R. G. Smith. Optical power handling capacity of low loss optical fibers as determined by stimulated raman and brillouin scattering. Appl. Opt., 11(11):2489–2494, Nov 1972.